AN ABSTRACT OF THE THESIS OF

Lillian F. Miles for the degree of Master of Science in Mechanical Engineering presented on June 8th, 2017.

Title: A Permanent-Magnet Linear Generator Wave Energy Converter for Low Power Ocean Sensors

Abstract approved:

James M. Moum Brian K. Bay

Renewable energy sources are becoming increasingly important due to their low environmental impact and limitless nature. This thesis explores the design of a 250 mW permanent magnet linear generator wave energy converter to power ocean sensors. While many wave energy converters exist, this is a unique application because the wave energy device is neither at the surface nor at the seafloor and is a low power application. The permanent magnet linear generator detailed in this thesis would enable the continuous operation of ocean mixing sensors with minimal maintenance and intervention.

A Permanent-Magnet Linear Generator Wave Energy Converter for Low Power Ocean Sensors

by
Lillian F. Miles

A THESIS

submitted to

Oregon State University

in partial fulfillment of
the requirements for the
degree of

Master of Science

Presented June 8, 2017
Commencement June 2017

Master of Science thesis of Lillian F. Miles presented on June 8, 2017

APPROVED:

Co-Major Professor, representing Mechanical Engineering

Co-Major Professor, representing Mechanical Engineering

Head of the School of Mechanical, Industrial, and Manufacturing Engineering

Dean of the Graduate School

I understand that my thesis will become part of the permanent collection of Oregon State University libraries. My signature below authorizes release of my thesis to any reader upon request.

Lillian F. Miles, Author

ACKNOWLEDGEMENTS

This research was supported by the National Science Foundation and the Office of Naval Research. I would like to express sincere appreciation to Professor Jim Moum for his technical assistance in oceanography, Dr. Julia Zhang for her power electronics guidance, Dr. Brian Bay for his mechanical engineering expertise, and my lab mates and colleagues for their assistance.

I would like to thank my family. My mom, Donna, showed me limitless support in my educational pursuits. Without her, this thesis would contain many more typos. I would like to thank my dad, Gino, who never fails to tell me how proud of me he is. I could not have done without my brother Jason's mixture of stress relieving weekends watching the Sounders and SolidWorks tutorials. My brother Daniel always ensured his support was felt even from across the pond. Finally yet importantly, I would like to thank my partner, Graham, for patiently listening to all of my doubts before banishing them.

TABLE OF CONTENTS

LIST OF FIGURES

LIST OF FIGURES (CONTINUED)

LIST OF FIGURES (CONTINUED)

LIST OF TABLES

A Low Power Permanent-Magnet Linear Generator Wave Energy Converter for Ocean Sensors

1. Introduction

1.1 Project Motivation

Oregon State University Ocean Mixing Group, led by Dr. Jim Moum, develops and implements instrumentation known as chipods, for detailed observations of small-scale ocean mixing processes. Currently, the chipods are powered by a stack of thirty-six D-cell lithium batteries limiting the deployment time of the chipods to approximately one year. The lithium batteries also pose a hazard as they are volatile and are stored in a water tight pressure case. Due to this volatility, the chipods are difficult to ship for international deployment. The large stack of batteries is heavy and takes up a sizeable amount of instrument space as well. All of the above contributes to the motivation to develop and implement a small scale wave energy generator to power the chipods.

1.2 Background and Current Wave Energy Technologies

There is both potential energy and kinetic energy stored in ocean waves. Wave energy converters aim at harnessing this mechanical energy to convert it to electrical energy. Wave energy has a power density of approximately 30 kW/m compared to other renewable energy sources (photovoltaics 150 W/m^2 and 600 W/m^2), allowing for more power extraction for smaller devices [1]. Wave energy is categorized by speeds typically less than 1 m/s and forces up to 1 MN. The main challenges facing wave energy devices are survivability in harsh ocean conditions due to high forces present and the highly corrosive environment, together with high operational and maintenance costs of any ocean device.

Wave energy devices can be categorized as oscillating body, overtopping, oscillating water column, or submerged pressure differential. Oscillating body wave energy devices can be further classified according to their power take off method as point

absorbers, attenuator, hinged flap or horizontal pendulum [2]. Oscillating body devices are typically direct-drive devices in which the mechanical part caused to move by the ocean waves is directly coupled to a reciprocating electrical generator. Current industry examples of each of these types of oscillating body wave energy converters are discussed in further detail below.

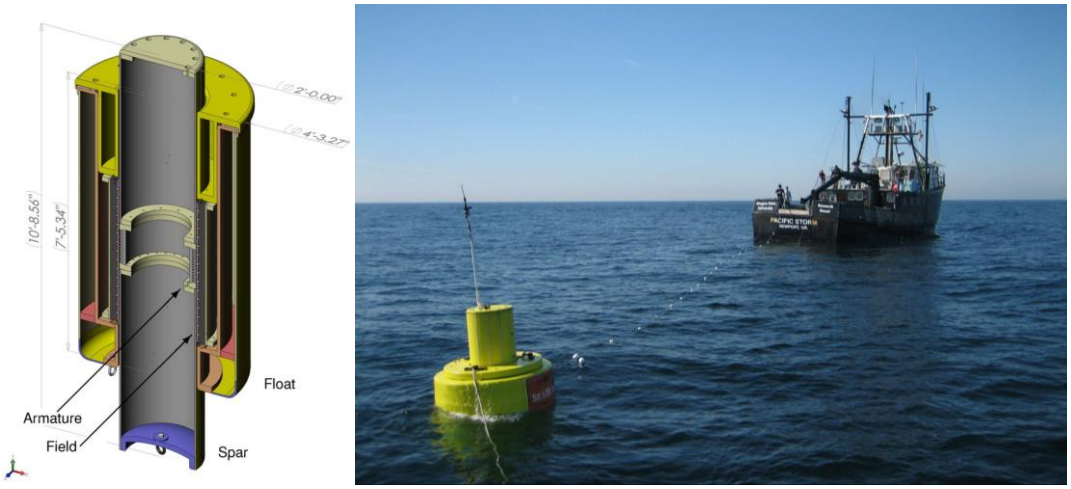

Figure 1: SeaBeav Wave Energy Converter [3]

Point absorber wave energy converters are typically moored devices consisting of two separate components, one rigidly attached to the sea floor and one attached to an oscillating buoyant float. The heave motion of the waves creates a relative mechanical motion of the two components that is coupled to an electric generator. Oregon State University's Permanent-Magnet Tubular Linear Generator (PMTLG) SeaBeav [4] is an example of a point absorber wave energy converter. The SeaBeav aims to produce 1 kW of power and consists of a spar containing three-phase armature windings that is moored to the sea floor. Surrounding the spar are rings of radially magnetized arc segment magnets inside a buoyant surface float, as shown in Figure 1 above [3].

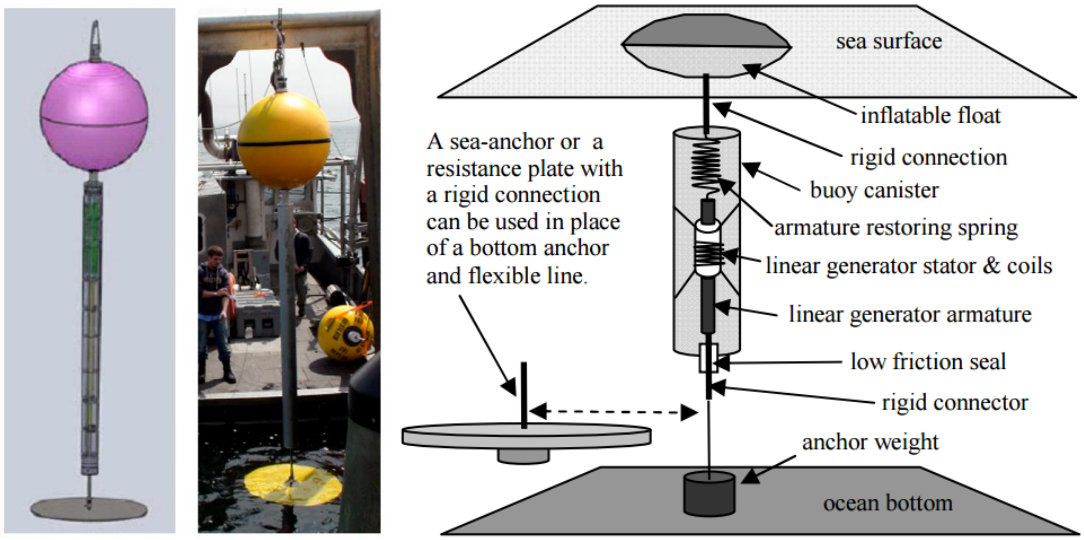

Figure 2: DC2 Wave Energy Converter [5] [6]

University of Rhode Island (URI) and Electro Standards Laboratory developed a low power (approximately 5 W) permanent magnet linear electric generator, called DC2, to power ocean sensors [5]. This generator utilizes axially magnetized cylindrical magnets connected to a drag resistance platform. Surrounding the magnets are three-phase windings that are rigidly connected to a buoyant surface float. Other examples of point absorber wave energy converters include PowerBouy^{TM} [7], WET-NZ [8], AquaBuOY [9], Wavebob [10], SeaRay [11], StingRAY [12], Lopf [13], Wavestar [14], and Seabased [15].

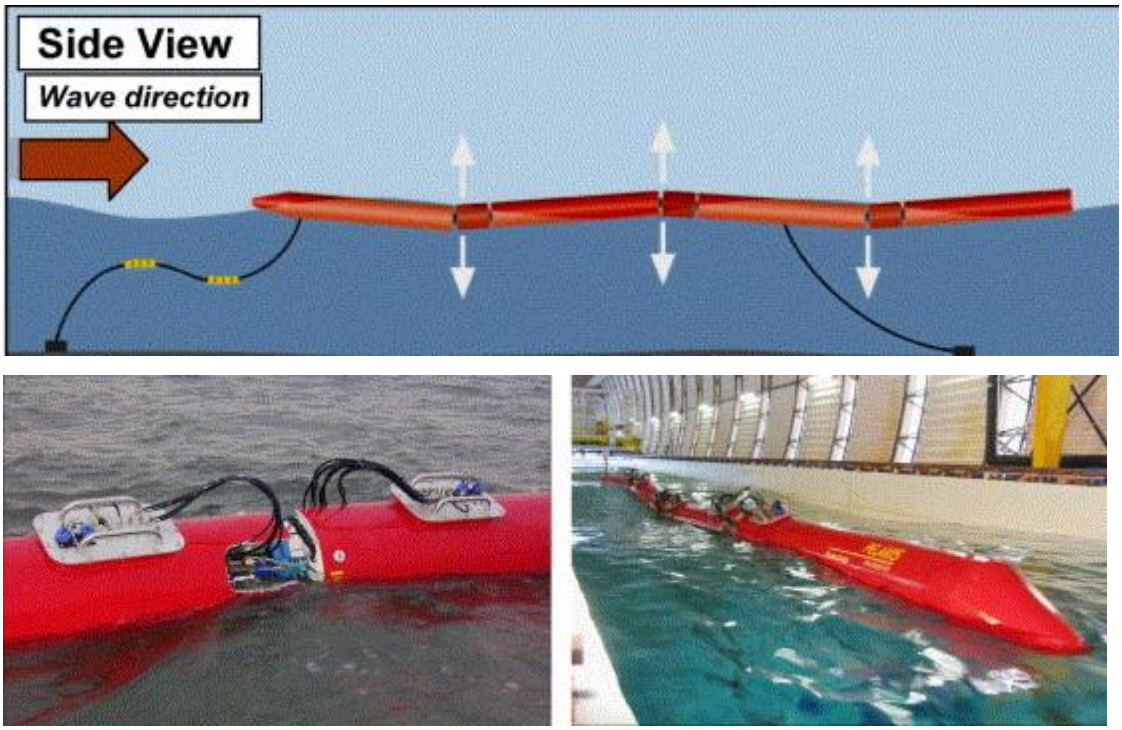

Figure 3: Pelamis Wave Energy Converter [16]

Attenuator wave energy converters float on the ocean surface aligned along the wave direction. As the wave propagates through the device, the different surface floating sections of the converter are moved relative to each other. An example of an attenuator wave energy converter is the Pelamis that produces approximately 750 kW of power [17]. The Pelamis is composed of several partially submerged cylindrical sections that are connected at each joint with hydraulic pistons. The relative motion of each cylindrical section to the adjoining section drives the hydraulic pistons [16]. Another example of an attenuator wave energy converter is the Dexawave [18].

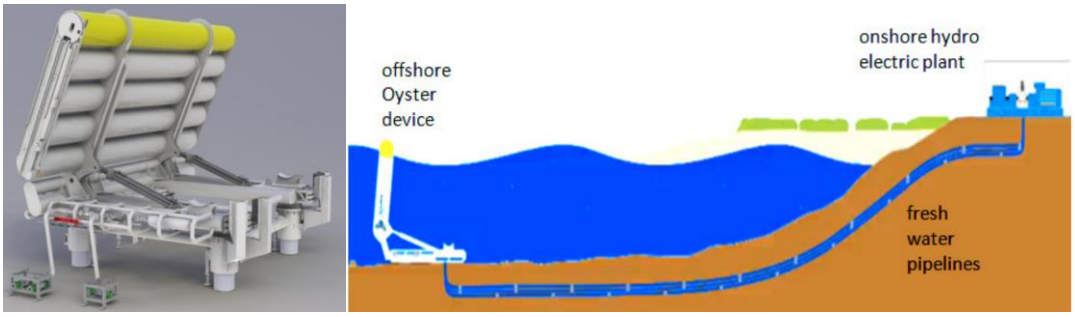

Figure 4: Oyster Wave Energy Converter [19]

Hinged flap converters, also known as oscillating water surge converters, utilize a drag flap on a vertical pendulum arm that moves with ocean surges. They are typically located in shallow water. The Aquamarine Oyster shown above in Figure 4 is an example of a hinged flap wave energy converter for ocean depths of 10 to 15 meters, with a goal to produce 2.4 MW of power. The buoyant hinged flap oscillates with the ocean waves to drive two hydraulic pistons connected to a frame bolted to the sea floor. The close proximity to the shore allows for hydraulic power transmission to an onshore hydroelectric plant [19]. Other examples of a hinged flap wave energy converter are BioWave [20], SurgeWEC [21], Wave Roller [22], EB Frond Wave Energy Converter [23], and Langlee [24].

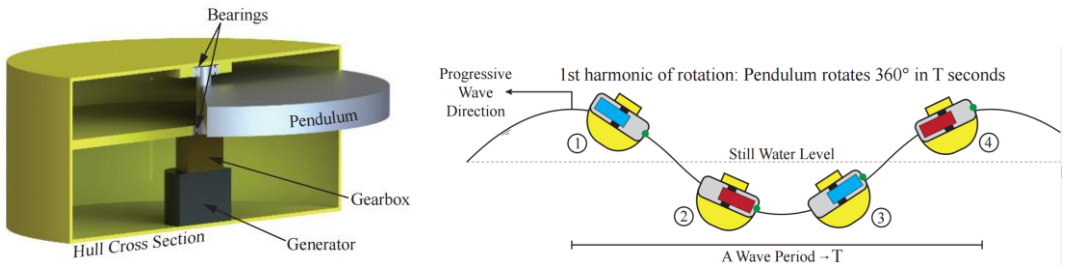

Figure 5: OSU's Vertical Axis Pendulum Wave Energy Converters [25]

Horizontal pendulum surface wave energy converters, also known as rotation mass wave energy converters or vertical axis pendulum wave energy converters, contain a horizontal rod with a mass on the end that rotates along the circumference with the heave and sway of the device. Oregon State University developed a vertical axis pendulum wave energy converter for approximately 60 kW that can be seen in Figure

5 above [25]. The Wello Penguin is another example of a horizontal pendulum device [26].

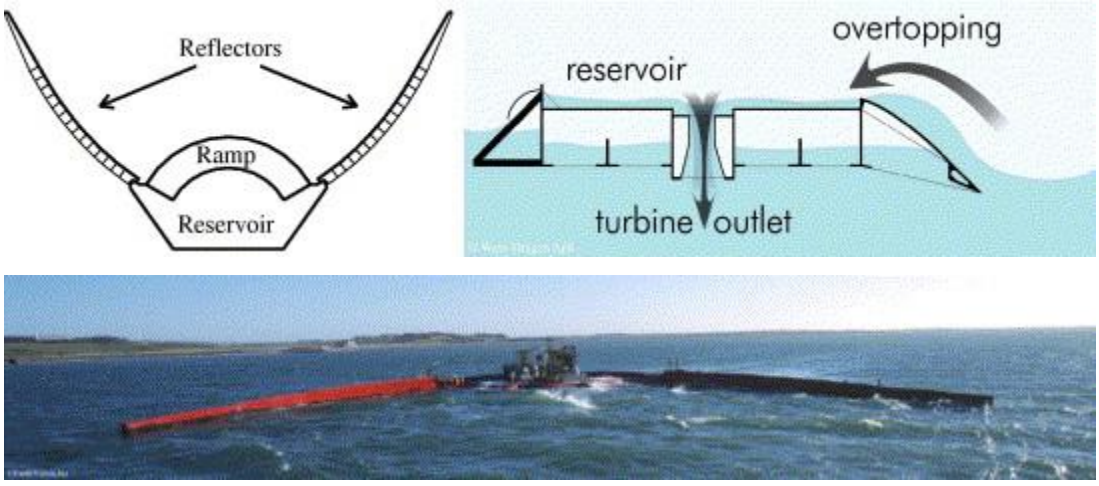

Figure 6: Wave Dragon Overtopping Wave Energy Converter [27]

Overtopping devices, also known as spill over devices, collect waves that are then forced upwards through a channel. This forced water passes through a hydroelectric low-head Kaplan turbine before returning to the ocean. The Wave Dragon is an example of an overtopping device that comes in variable sizes for power outputs from 250 to 940 kW [27]. The Wave Dragon concept can be seen in Figure 6, together with a real photo of a deployed Wave Dragon [27]. The WavePlane is another example of an overtopping wave energy converter [28].

Figure 7: LIMPET Wave Energy Converter [29]

Oscillating water column devices utilize a chamber with one side submerged in the ocean and the other side open to the surrounding air, with a wind turbine at the opening of the air side of the chamber. The periodic waves force the water level in the chamber to oscillate, pushing air in and out of the chamber, powering the wind turbine [29]. LIMPET is an onshore oscillating waver column wave energy converter containing two 250 kW wind turbines [30]. Oceanlinx, an Australian based company, makes three different wave energy converters: GreenWave [31], OgWave [32], and BlueWave [33] that are additional examples of commercially available oscillating water column devices.

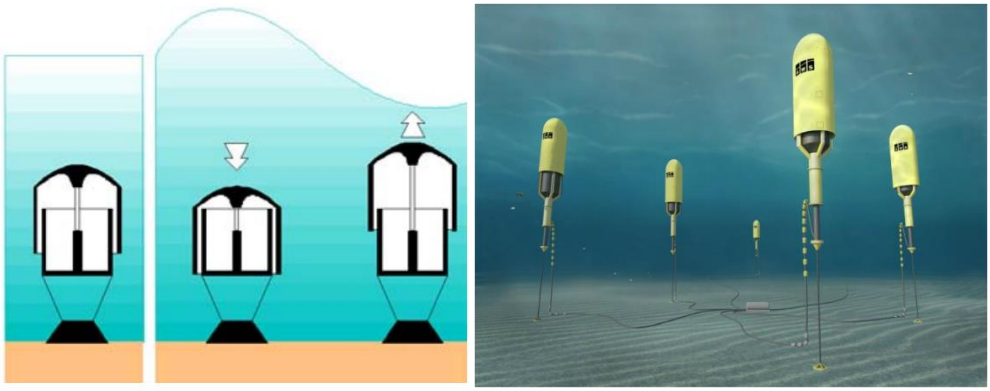

Figure 8: Archimedes Wave Swing [34] [35]

Submerged pressure differential devices are attached to the seabed. The ocean waves cause the water depth to oscillate, creating a pressure differential that drives a linear generator. Submerged pressure differential devices are typically located in shallow waters near shores and are used to either desalinate water or export grid energy [2]. They require tuning for varying ocean wave heights for the greatest efficiency [36]. The Archimedes Wave Swing (AWS) is an example of a 25-250 kW [35] submerged pressure differential device and can be seen in Figure 8 above [35, 36]. Cylindrical Energy Transfer Oscillator (CETO) [37] is another example of a submerged pressure differential device. AWS uses a permanent magnet linear electric generator while CETO uses hydraulic pumps.

1.3. Design Objectives

The chipods need and average of 250 milliwatts of power at 7.2 volts DC. The resistive load of the chipod varies but the average load is 206 Ω. The wave energy converter needs to be able to supply continuous power at the rated voltage to the chipods in any ocean condition for 18 months with no intervention. Current chipods are deployed with accelerometers. Analyzing this accelerometer data provides a heave velocity range for the chipods of 0.3 m/s to 3 m/s. The chipods are deployed at varying depths from 10m to 200m on a moored cable system to the sea floor. The top section of the moored cable is made of rigid steel-jacketed cable that does not stretch while the remainder of the cable is made of ¾ inch diameter nylon that stretches. The moored system is deployed so that the surface float stretches the cable to maintain roughly 1000 pounds of tension at all times. This keeps the moored cable taught and close to vertical in the ocean. An example moored cable system can be seen below in Figure 9.

Running power cables parallel to the mooring cable for large distances is not a option. In the past, the Ocean Mixing group at OSU has experienced difficulties with entanglement of cables while deploying from its ships and during use of the mooring system in the ocean. Fatigue wear has also caused loss of conduction in power cables. Based on prior experience difficulties, the new wave energy device must be able to produce power at the location of the chipod. The wave energy converter must also be able to withstand the harsh ocean environment including corrosion, varying pressures with depths, schooling fish and other marine life interferences or growths, varying wave conditions, and varying temperatures from -2°C to 35°C. The customer requirements are summarized in Table A below.

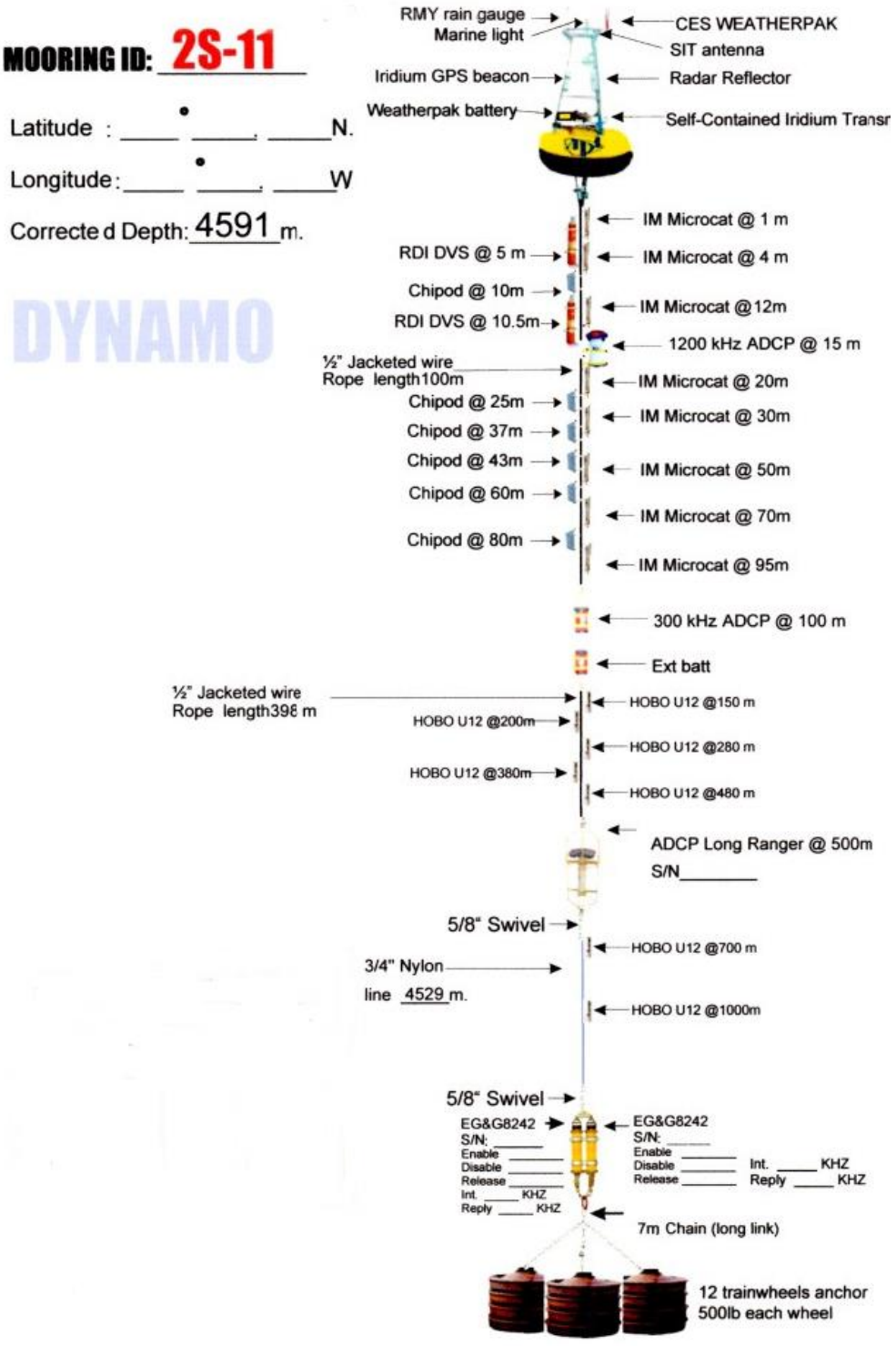

Figure 9: Chipod Mooring System

Customer Requirements	**Quantification**
Minimum Continuous Power	250 mW
Constant Voltage Supplied	7.2 V
Life Span Without Maintenance	18 months
Operation Temperature Range	-2°C to 35°C
Operate in Varying Ocean Conditions	0.3 m/s to 3 m/s heave velocity
Operate in Varying Ocean Depths	10-200 m deep
	200 kPa to 2 MPa of pressure
Chipod and Power Device are at the Same Location	N/A
Must Withstand Harsh Ocean Conditions	N/A

Table A: Customer Requirements

1.4. Project Background and Literature Synthesis

At 200m deep, the ocean waves no longer have an effect apart from an induced pressure differential. The available motion sources for a wave converter are ocean currents and the relative motion of the rigid steel-jacketed cable of the mooring system to the linearly stagnant ocean water. Many of the wave energy converters discussed above operate at the surface of the ocean with fewer devices located near the seabed in shallower waters. The novelty of this project lies in the device being located at neither the surface nor the seabed and at varying ocean depths. Submerged pressure differential devices are also located mid ocean.

Since the chipods are deployed on the rigid section of the steel-jacketed cable, the distance between the chipods and the ocean surface remains constant regardless of the wave height. There is little to no pressure differential for a wave energy converter connected to the moored cable at the chipod level. Additionally, most other wave energy converters are for much higher power output than what the chipod needs. The exception is the URI DC-2 wave energy converter [5].

Another Oregon State Masters student, Molly Stieber, worked on this generator project in 2015. Four different design concepts were generated including a rocker

dyad, a linear generator, a spinner device, and an eel piezoelectric device [38]. The rocker dyad was a 4 bar mechanism device that would rotate with drag through the water. The linear generator investigated involved back driving a linear actuator that contained a stepper motor. The spinner device was essentially a paddle that would drag in the ocean to cause it to spin. The piezoelectric eel idea would have operated with ocean currents instead of translated heave motion to move underwater sheets of piezoelectric material [2]. The spinner design was unsuccessful because it would have needed an extremely large paddle to create the large forces required to back drive the motor at low speeds [38]. Back driving a linear actuator that still used a rotational motor (converting the linear motion to a rotational motion using a mechanical interface) was unsuccessful also because it, too, had a large initial back drive force requiring a large drag platform. Both of the design attempts previously investigated were not direct drive wave energy converters [38].

Direct drive wave energy converters do not require a mechanical interface between the wave energy converter and the electrical generator. This can simplify the design by reducing the number of moving components and increase the efficiency [2]. There has been an increasing trend in the number of direct drive wave energy converters due to their lower maintenance costs, simplicity, and higher efficiencies [2]. Direct drive wave energy converters are typically linear systems.

There are four different linear generators that are suitable for wave energy converters: induction generators, synchronous generators with electrical excitation, switched reluctance generators, and permanent magnet synchronous generators [39]. Polinder et al., investigated the different generator options used in wave energy converters and direct drive wind turbines and concluded that permanent magnet synchronous generators are the best generators for wave energy converters [40, 34, 2].

Additionally, a cylindrical generator would reduce the forces placed upon generators' bearings as the magnetic forces are axially symmetric [39]. Based upon the lessons

learned in conducting this literature review, the best suitable design for a wave energy converter to power the chipods is a cylindrical permanent magnet linear synchronous generator. These types of generators are employed in the AWS, SeaBeav, and URI's DC-2, among others [35, 6, 11, 5, 40, 39, 34, 3, 4, 12].

2. Methods

2.1. PMLG First Approximation

According to Faraday's Law, for a linear generator with a constant magnetic field orthogonal to the windings the induced voltage in the winding is:

$$EMF = -N\frac{d\Phi_B}{dt} = Blu$$

where EMF is the induced voltage, N is the number of windings, Φ_B is the magnetic flux, B is the magnetic field, l is the length of copper wire, and u is the relative linear velocity between the copper windings and the magnetic field. According to Lorentz force law, for a same orthogonal generator with a negligible electric field the force to move the windings relative to the magnets is:

$$F = q\left(\vec{u} \times \vec{B}\right) = Bil$$

where q is the charge of a particle, u is the velocity of the charge particle, i is the resulting current through the copper winding, and l is the length of the copper wire. The mechanical drag force equation is:

$$F_D = \frac{1}{2}C_D\rho u^2 A$$

where F_D is the drag force, C_D is the coefficient of drag taken to be 1.9 for a flat plate [41], ρ is the density of seawater (1027 kg/m^3), and A is the square area of the flat drag plate.

Combining the above equations using the parameters given below in Table B, the square area of the drag platform, output voltage, output current, generator power, and the number of windings can be approximated through a MATLAB Simulink script. The velocity for the generator is approximated using the velocity data from a typical chipod limited by the stroke of the generator. This Simulink model can be seen in Figure 10 below; the MATLAB script is attached in Appendix A.

Defined Constant Inputs	Value
Constant Magnetic Field	0.25 T
Length of Copper Wire	120 m
Stroke Length of Generator	0.4 m
Diameter of Copper Windings	1.5 in
Drag Coefficient, C_D	1.9
Seawater density,ρ	1027 kg/m^3
Chipod Average Resistive Load	206 Ω

Table B: Initial Wave Energy Converter Model Inputs

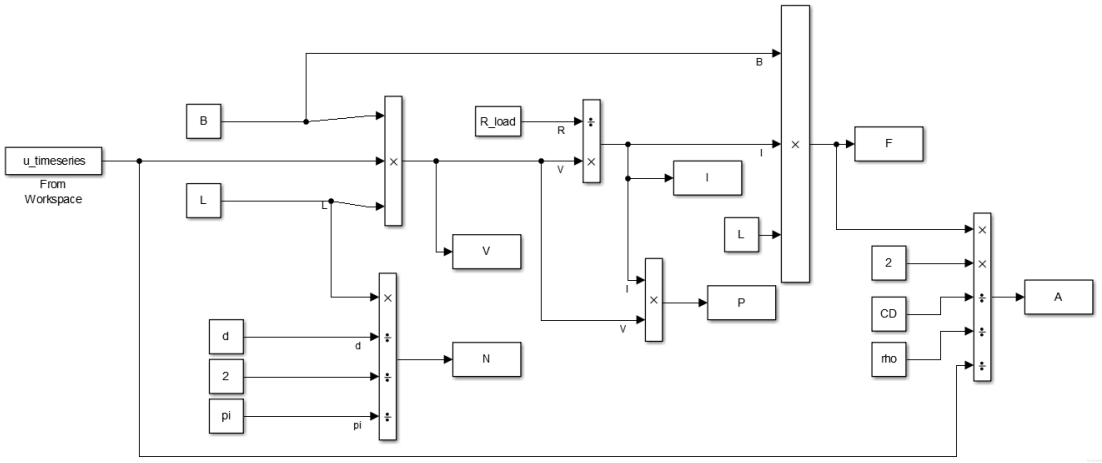

Figure 10: Initial Wave Energy Converter Approximation Simulink Model

The results of the initial model is shown in Table C below and Figures 11-13.

Model Constant Outputs	Value
Number of Windings, N	502
Drag Plate Area, A	0.0045 m^2
Average Power	322.30 mW

Table C: Initial Wave Energy Converter Model Outputs

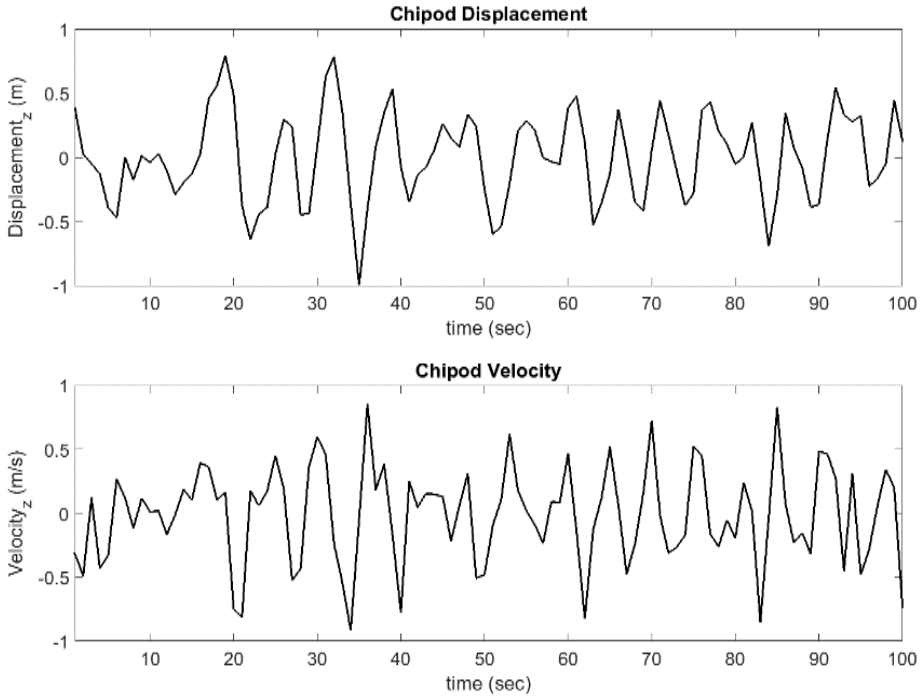

Figure 11: Displacement and Velocity of a Typical Chipod Sensor

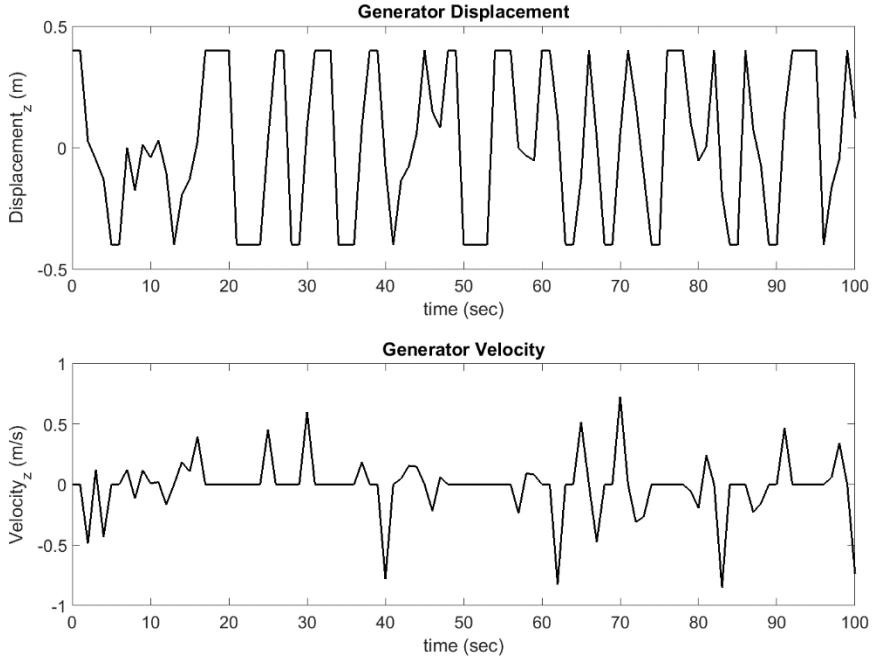

Figure 12: Generator Displacement and Linear Velocity

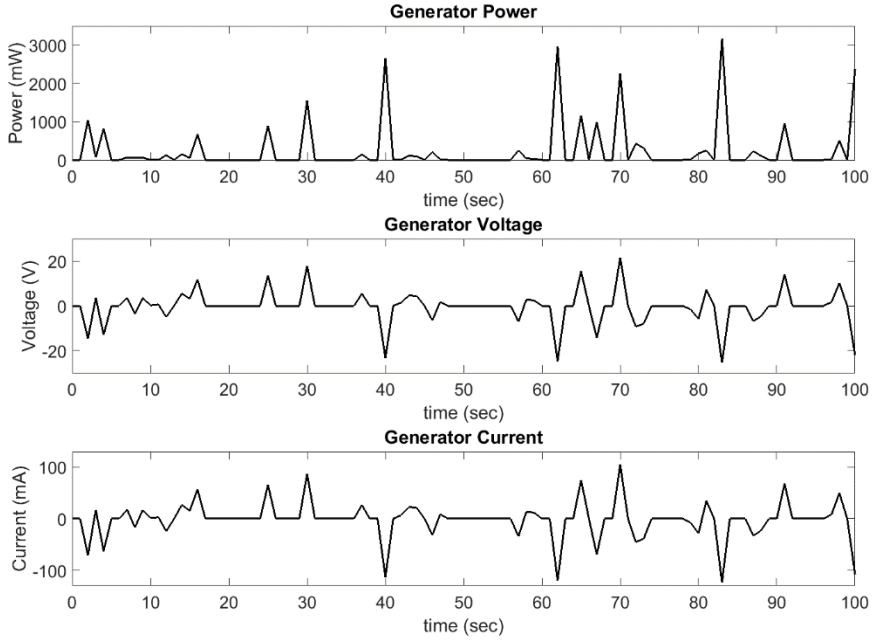

Figure 13: Generator Output Power, Voltage, and Current

This initial model presents one possible solution for a generator to produce at least 250 mW. However, this model assumes a constant magnetic field which is not realistic with permanent magnet linear generators. To properly model the magnetic field, a Finite Element Analysis model in Ansys Maxwell is needed. This model also assumes the displacement and relative velocity of the magnet and the coils directly follows the observed linear displacement and velocity of the chipod as long as the chipod displacement is within the stroke of the linear generator. If the chipod displacement is outside of the stroke of the generator, the velocity of the magnets relative to the coils is assumed to be zero. In practice, there would be a delay and loss of some displacement for a drag plate attached to the generator.

2.2. Static Maxwell 2D Model

In the PMLG described in URI DC-2 generator [5], the cylindrical magnets used were axially magnetized. However, in larger scaled PMLG, such as OSU's SeaBeav [3],

radially magnetized magnets are used. The reason for that may be that larger generator's axially magnetized ring magnets or cylindrical magnets are extremely costly and are not readily commercially available. For a smaller generator, both cylinder and ring magnets are affordable and commercially available.

From Faraday's Law, voltage is produced when magnetic windings pass through a change in magnetic flux. For axially magnetized magnets, there were concerns that the winding would not pass through enough change in magnetic flux to produce power efficiently because the windings would travel parallel to the magnetic flux lines. It was unknown how the core of the generator and the windings would alter the magnetic field and flux lines. Without the core, the magnetic field and flux lines are easy to envision.

Consider the magnetic field and flux lines shown in Figure 14 below for a 3 inch outer diameter, 2 inch inner diameter, and 1 inch thick NdFeB, Grade N42 magnet [42].

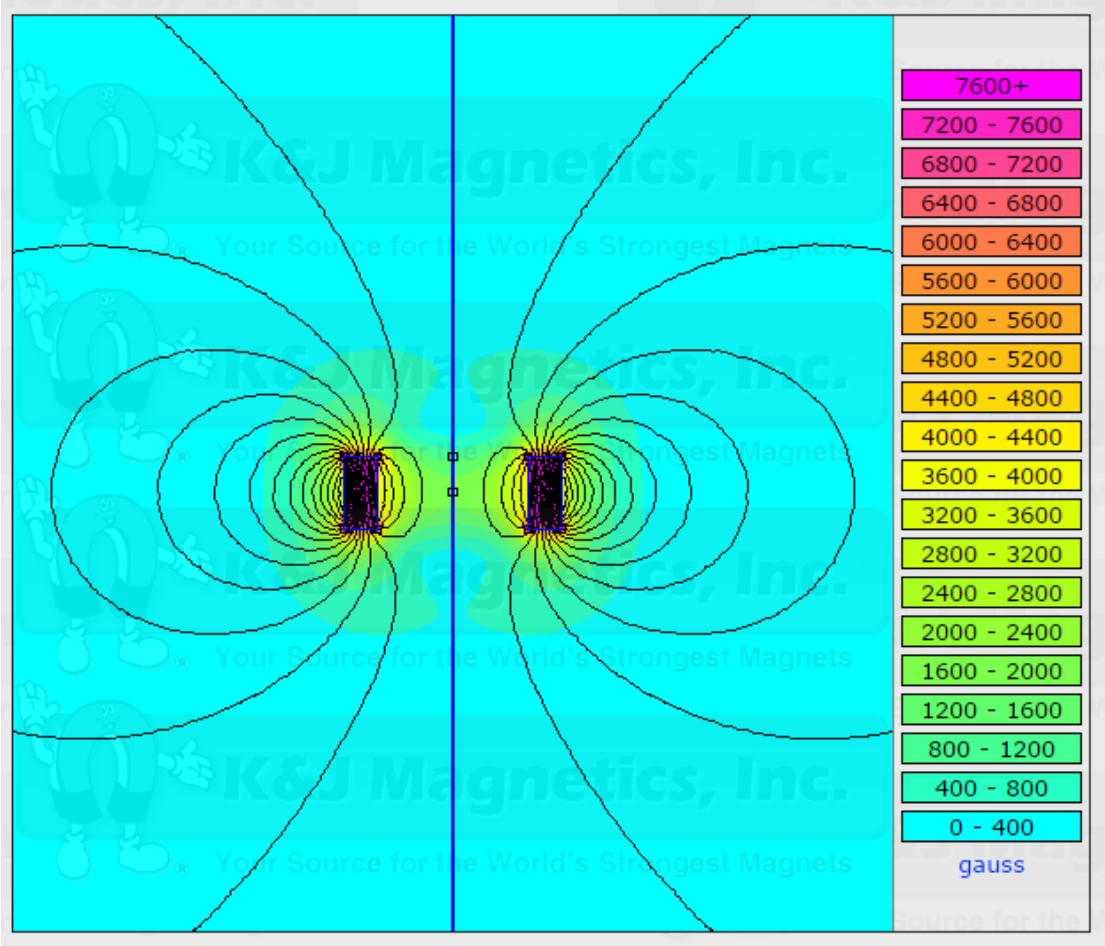

Figure 14: Cross Sectional View of a Ring Magnet's Magnetic Field and Flux Lines [42]

For a winding moving through the inner radius of the ring magnet, it is very difficult to hypothesize how the magnetic field and flux lines will change. To investigate this, a 2-D Maxwell model was performed to measure the magnetic field and magnetic flux line of an axially magnetized ring magnet moving around copper windings. For the simulation, five 3 inch outer diameter, 2 inch inner diameter, and ½ inch thick NdFeB, Grade N42 axially magnetized magnets stacked in alternating polar directions spaced ½ apart were placed around a 1.5 inch diameter iron core. The magnets were spaced equally apart to match URI's generator DC-2, attempting to achieve a sinusoidal power output. The windings were not included as their effect is

considered negligible compared to the iron core, since copper is not very magnetic. The results of the model are shown below in Figure 15.

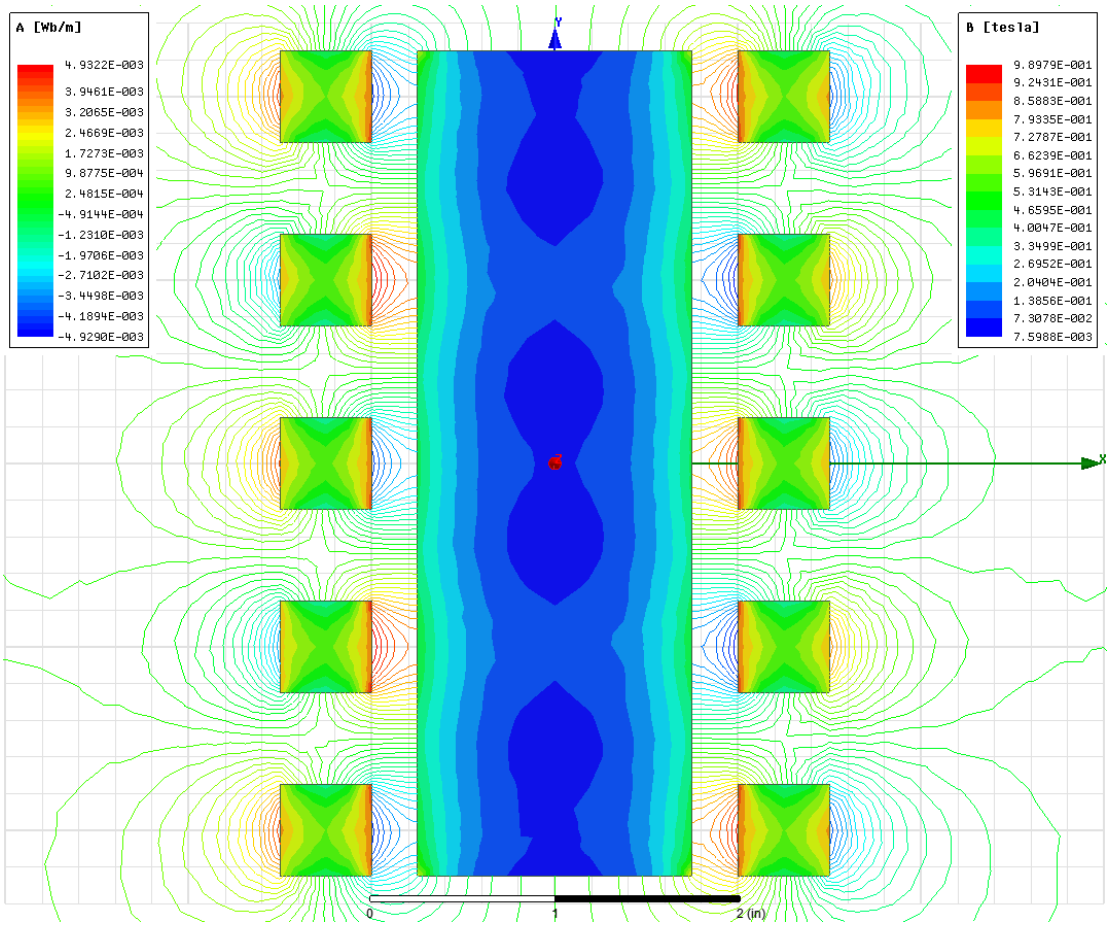

Figure 15: 2-D Axially Magnetized Ring Magnets Magnetic Field and Flux Around Iron Core

The magnetic flux lines were significantly altered with the iron core and the magnet-to-magnet interactions to align the flux lines orthogonal to the windings linear velocity. This allowed for axially magnetized magnets to produce power efficiently at this size.

2.3. Transient Maxwell 3D Model – Cylinder Magnets or Ring Magnets

Next, a transient model to compare two different possible configurations was made, one with cylindrical magnets on the inside passing through coils on the outside

similar to URI's DC-2 generator [5], the second with ring magnets on the outside with coils passing through on the inside. Starting and finishing positions of cylinder magnet and ring magnet generator prototypes are shown below in Figures 16 and 17 respectively. The copper magnetic wire is the orange color, the magnets are dark grey and the iron core is light grey.

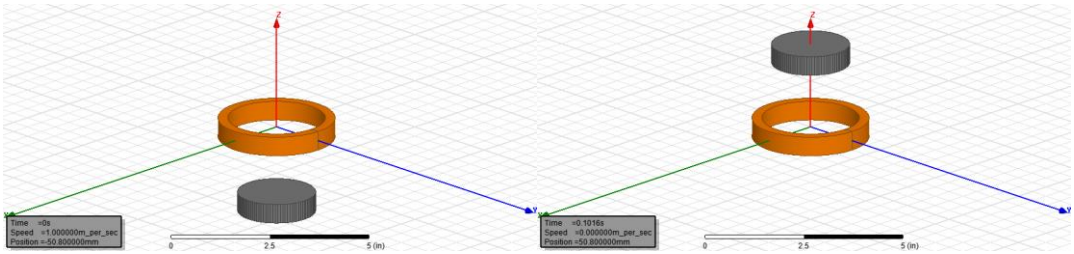

Figure 16: Transient Cylindrical Magnet Simulation Starting and Finishing Positions Respectively

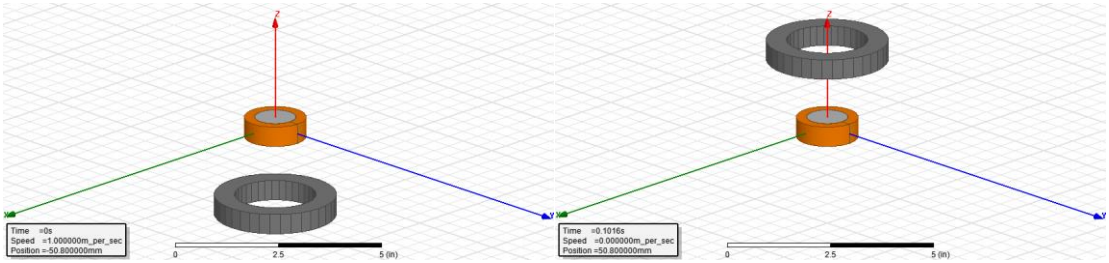

Figure 17: Transient Ring Magnet Simulation Starting and Finishing Positions Respectively

To be able to make a direct comparison between the two different configurations, the overall size of the generators was the same. Table D immediately below outlines the constants across the two models and Table E further below outlines the differences between the two models.

Constants Across Both Simulations	
Magnet to Winding Relative Linear Velocity	1 m/s
Stroke Length	4 inches
Total Generator Outer Diameter	3 inches
Magnet Height	1/2 inch
Coil Height	1/2 inch
Air Gap	1/4 inch
Length of Copper Magnet Wire	706.85 inches
NdFeB Grade	N42
Load Resistance	206 Ohms
Maxwell Step Size	0.01s

Table D: Constants across Cylinder and Ring Magnet Simulations

Differences Between Simulations			
Cylinder Magnet		**Ring Magnet**	
Cylinder Magnet Geometry	2 inch Diameter	Ring Magnet Geometry	2 inch Inner Diameter 3 inch Outer Diameter
No Iron Core		Iron Core	1 inch diameter 1/2 inch height
Coil Diameter	2.5 inches	Coil Diameter	1.5 inches
Number of Coils	90	Number of Coils	150

Table E: Differences between Cylinder and Ring Magnet Simulations

The Ansys Maxwell model outputs the induced voltage and current through the winding. The resulting power of each generator model can be seen in Figure 18 below.

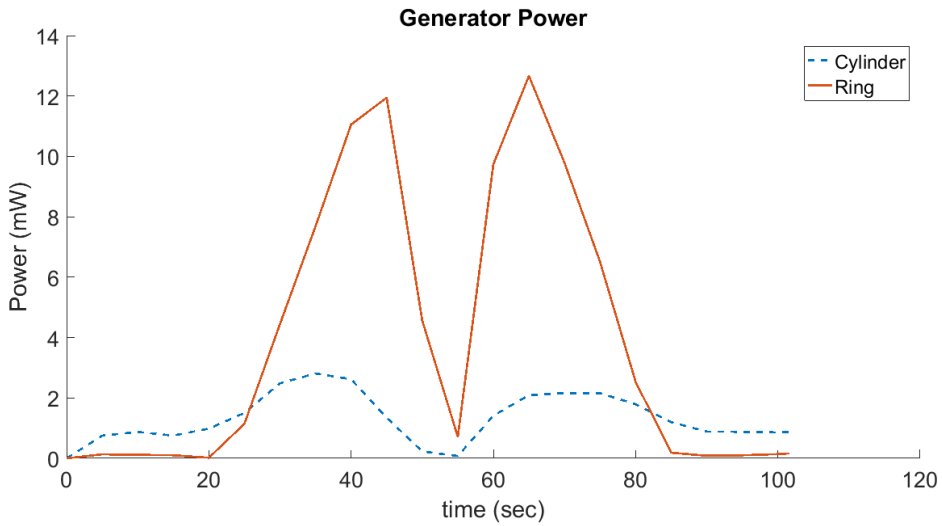

Figure 18: Power Comparison between Cylinder Magnet and Ring Magnet Generators

The sharpness seen in the above power curve is due to the relatively large step size of the simulation. However, a quick comparison to determine which generator option produces more power shows that the ring magnet generator is the clear winner, producing 296.86% more energy. A permanent ring magnet tubular linear generator is the better choice for this application over a permanent cylinder magnet tubular linear generator like URI's DC-2 generator. In addition, having the coils on the inside of the magnet allows them to be stationary in relation to the chipod. Rigidly attaching the coils to the mooring prevents fatigue wear of the power take off cable [3]. The only disadvantage to this is that large ring magnets are approximately twice as expensive as cylinder magnets [42].

2.4. Transient Maxwell 3D Model –Ring Magnet Thickness

There are two commercially available 3 inch outer diameter, 2 inch inner diameter magnets in ½ inch thick and 1 inch thick. Since the flux lines are compressed and condensed between the magnets, due to magnet-to-magnet interaction, it was hypothesized that using an increased number of thinner magnets would produce more power than using fewer thicker magnets, as well as reduce the overall cost. To investigate this, another comparison Maxwell simulation study was performed. In the

first simulation, one 1 inch thick ring magnet was used together with one 1 inch high winding containing 150 coils (referred to hereafter as 1x1inch). In the second simulation, two 1/2 inch thick ring magnets were used, together with two ½ inch high windings containing 75 coils each, 150 total (referred to hereafter as 2x1/2 inch). The generator height is considered to be the height required for the magnet stack to pass completely over the winding stack. The starting and finishing positions of the 1x1inch and the 2x1/2 inch simulations can be seen below in Figures 19 and 20 respectively. The similarities and differences between the two simulations are summarized in Tables F and G further below.

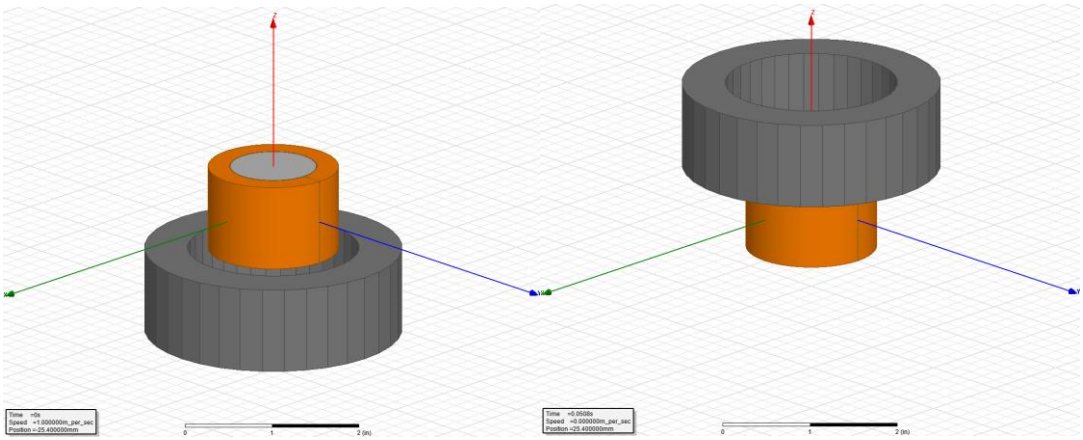

Figure 19: Transient 1x1inch Simulation Starting and Finishing Positions Respectively

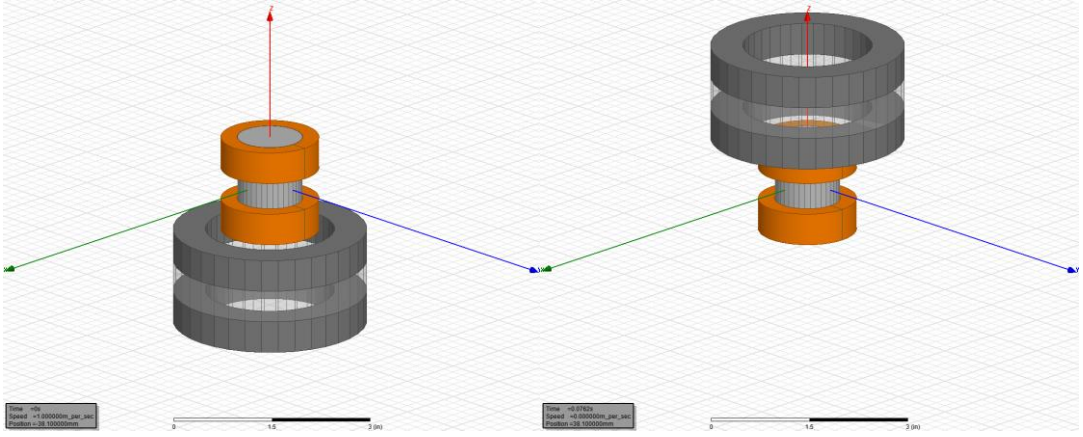

Figure 20: Transient 2x1/2inch Simulation Starting and Finishing Positions Respectively

Constants Across Both Simulations	
Magnet to Winding Relative Linear Velocity	1 m/s
Ring Magnet Outer Diameter	3 inches
Ring Magnet Inner Diameter	2 inches
Iron Core Diameter	1 inch
Coil Outer Diameter	1.5 inches
Air Gap	1/4 inch
Length of Copper Wire, l	706.85 inches
Number of coils	150
NdFeB Grade	N42
Load Resistance	206 Ohms
Maxwell Step Size	1ms

Table F: Constants Across 1x1inch and 2x1/2inch Simulations

Differences Between Simulations		
Parameters	**One 1 inch Thick Ring Magnet**	**Two 1/2 inch Thick Ring Magnets**
Number of Magnets	1	2
Magnet Thickness	1 inch	1/2 inch
Magnet Spacing	N/A	1/2 inch
Stroke Length	2 inches	3 inches
Generator Height	3 inches	4.5 inches
Number of Windings	1	2
Coil Height	1 inch	1/2 inch

Table G: Differences Between 1x1inch and 2x1/2inch Simulations

The windings of the 2x1/2 inch simulations were connected in series. The resulting power of the two simulations can be seen below in Figure 21. The power is shown against the magnet stack position to better demonstrate the two on one graph since they ran for different times (for 2x1/2 inch, the stroke is longer).

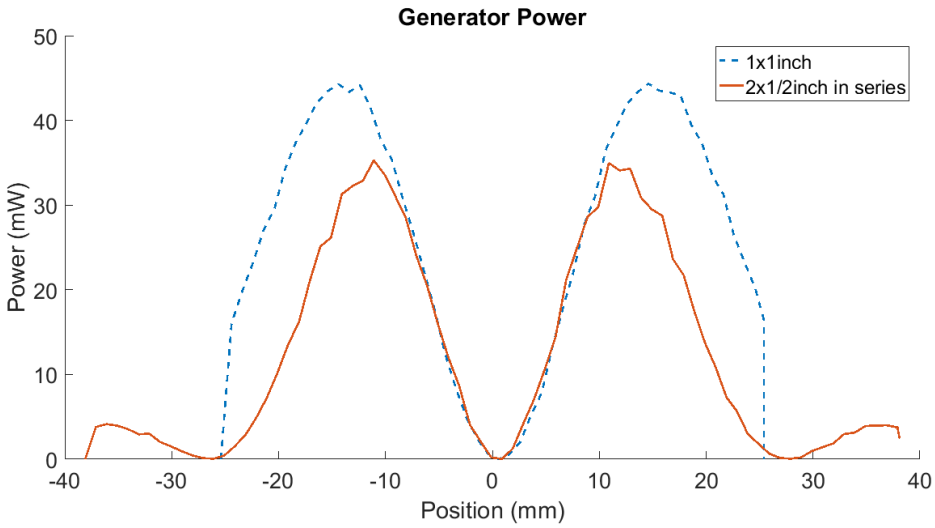

Figure 21: Generator Power for 1x1inch and 2x1/2inch Connected in Series Simulation

The initial power simulations results are misleading. The windings of the 2x1/2 inch simulations were initially connected in series but their voltages were out of phase. The result of connecting them in series made it so the current in each winding was the same; consequently, when the voltages were opposite signs, one of the windings was passing current to the other winding. The induced voltage in each winding can be seen below in Figure 22.

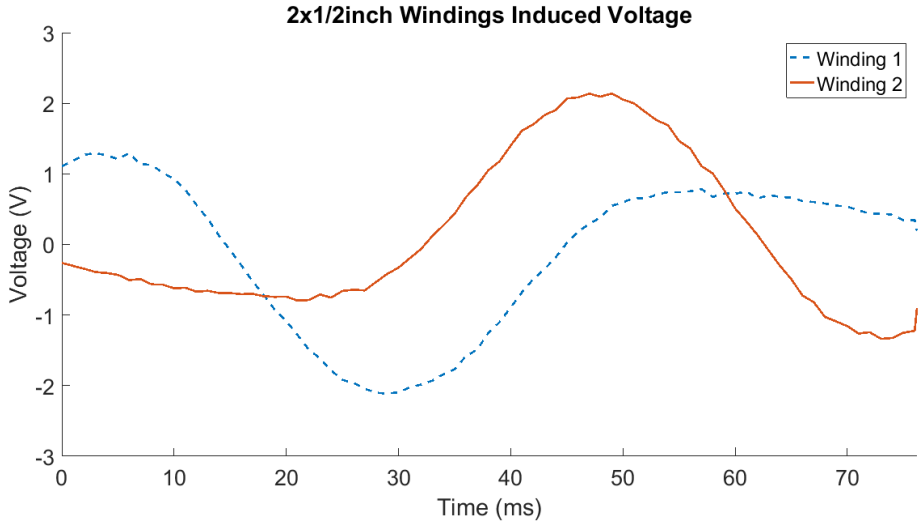

Figure 22: Windings Voltage for 2x1/2inch Simulations

Operating under the assumption that the induced voltages of the windings are in phase (i.e. the sign of the induced voltage is the same), the power can be calculated from the induced voltages from the simulation and Ohm's Law [43] shown below:

$$P = \frac{V^2}{R}$$

The power results of the second simulation accounting for the phase shift of the voltages can be seen below in Figure 23.

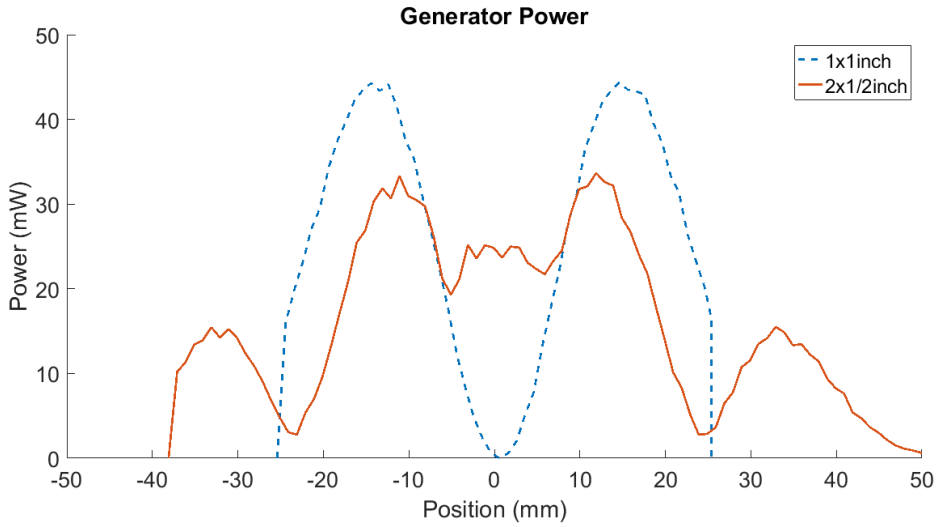

Figure 23: Generator Power for 1x1inch and 2x1/2inch in Phase Simulation

The energy generated for each configuration was similar. The power was more uniform in the 2x1/2 inch case. The ½ inch magnets are approximately a quarter of the price [44]. They will also be much easier and safer to handle in assembly due to the lower pull force associated with them. The thicker one inch magnets have a higher power density but the price of 4 ½ inch magnets is roughly the same as one 1 inch magnet. The ½ inch magnet thickness is the better choice for the initial investigation of the PMLG because they provide for a more uniform power distribution, they are more cost efficient, and they are easier and safer to handle.

2.5. Transient Maxwell 3D Model –Windings Spacing

The phase of the induced voltages of the windings is important. For a large generator with multiple windings, it would be advantageous to connect the windings in series so that only one AC/DC rectifier is needed. In order to do this, the induce voltages must be in phase as well as the current direction. According to Ampere's Law, the current direction will alternate as the polarity of the magnetic field changes when the magnets pass over the coil [43]. As such, alternating the polarity of the magnet stack and alternating the winding direction from clockwise to counter-clockwise will produce currents of the same sign.

During the investigation of magnet thickness, the problem of voltage phase surfaced. With equal magnet and equal windings spacing, it was hypothesized that the voltage would be sinusoidal in phase from winding to winding based on the findings from URI's DC-2 generator design [6]. The magnet height simulation shows that this is not the case. An iterative Maxwell simulation was performed varying the spacing between coils until the winding's induced voltages were in phase. Three ½ inch magnets were used. The spacing between windings that provided approximate voltage in phase was found to be 0.9 inches. The starting and ending positions of this simulation are presented below in Figure 24, together with the parameters of the simulation in Table H.

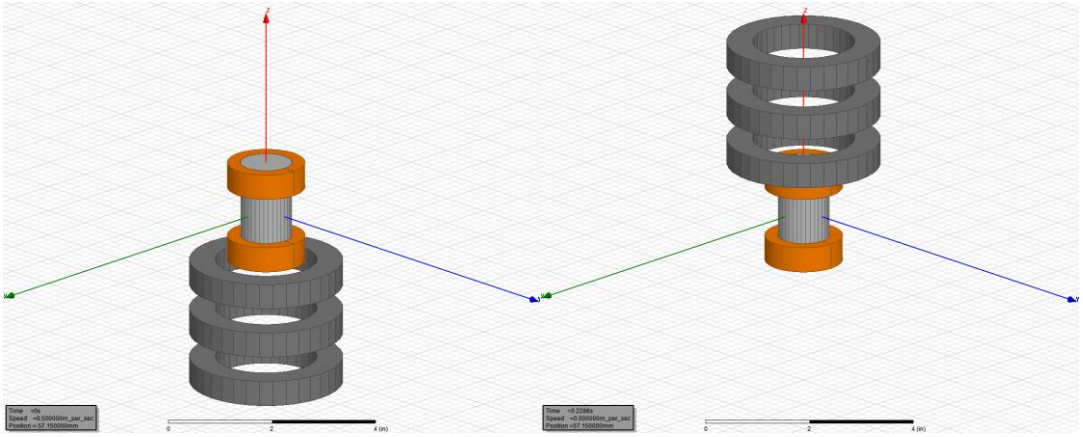

Figure 24: Transient Winding Spacing Simulation Starting and Finishing Positions Respectively

Parameters	Values
Magnet to Winding Relative Linear Velocity	1 m/s
Number of Magnets	3
Ring Magnet Outer Diameter	3 inches
Ring Magnet Inner Diameter	2 inches
Ring Magnet Height	1/2 inch
Iron Core Diameter	1 inch
Coil Outer Diameter	1.5 inches
Number of Windings	2
Windings Spacing	0.9 inches
Air Gap	1/4 inch
Length of Copper Wire, l	706.85 inches
Number of coils	150
NdFeB Grade	N42
Load Resistance	206 Ohms
Maxwell Step Size	1 ms

Table H: Parameters for Transient Winding Spacing Simulation

The induced voltages of the windings can be seen in Figure 25 below.

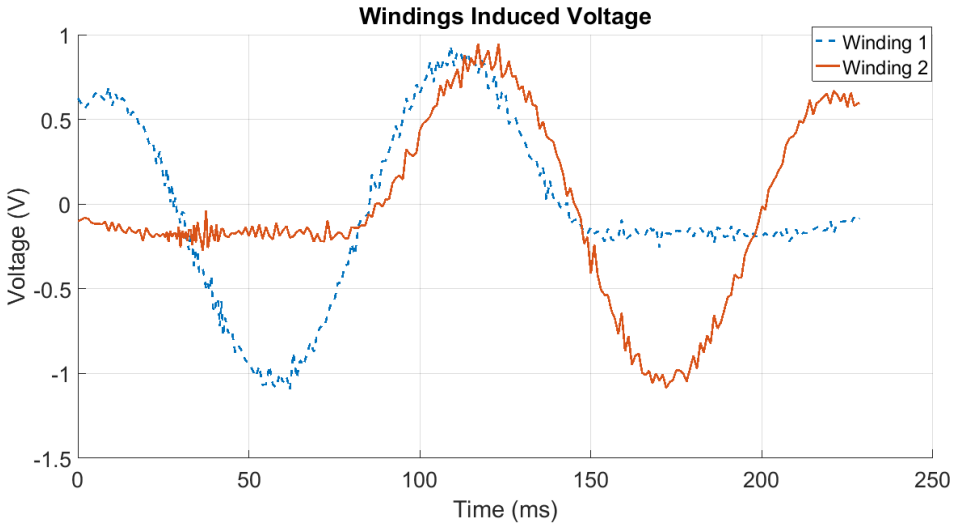

Figure 25: Windings Spacing Simulation Induced Voltage

Maxwell does not provide the ability to sweep geometric variables. The iterative solution to vary the spacing was very computationally expensive. The induced

winding voltages above are close enough to being in phase for this application. Further simulations could be performed to get the voltages exactly in phase.

3 Linear Test Bed

3.1 Design of Linear Test Bed

To verify the Maxwell simulations, an experimental testing rig was required. The goal of the test rig was to produce repeatable and measurable induced voltage waveforms for a scaled down generator from a known velocity input. These results could then be compared to the Maxwell simulations to ensure the accuracy of the Maxwell program. The linear test bed had to include the capability to alter the testing set up for multiple magnet stack configurations and multiple coil configurations. Additionally, the ability to vary the velocity input was desired.

There were multiple potential designs possible and commercial devices available to accomplish this test fixture. After reviewing commercially available linear actuators and getting an estimate for contracting out the design, it was decided that the rig should be built in house due to prohibitive costs of purchasing a commercial unit. There were two design concepts evaluated-- a four bar mechanism to convert a rotational motor to linear motion and a belted drive test rig. The belted drive system was chosen due to concerns about the stall positions of the four bar mechanism aligning with the increased force positions of the magnets moving around the coils and the iron core.

The magnet stack was rigidly attached to a ball bearing truck on a linear guide rail. The truck was then attached to the timing belt drive system. The belt encircled two pulleys [45], one mounted to a stepper motor key and one mounted on a shoulder screw. Next, the stator containing the iron core and windings was clamped in concentric alignment, with the motors for a ¼ inch air gap between the core and the magnets. The system was supported by an extruded aluminum bar. A picture of the linear test bed can be seen below in Figure 26, with detailed CAD drawings available in Appendix B.

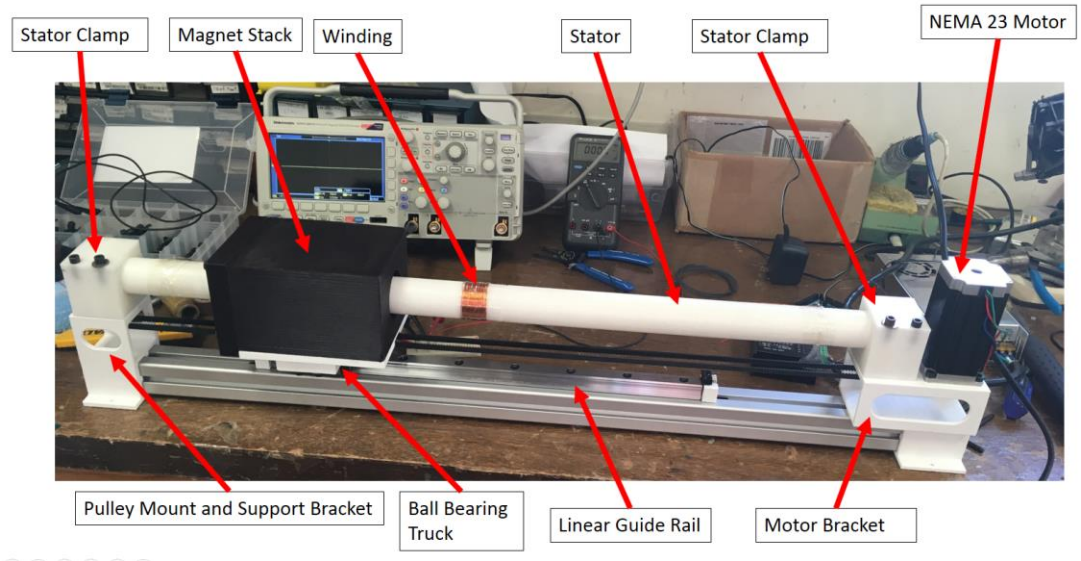

Figure 26: Linear Test Fixture

The torque characteristics of the test fixture were estimated using the force outputs of the Maxwell simulation for winding spacing, since the winding spacing was a good example of an experimental test. The force magnitude can be seen below in Figure 27.

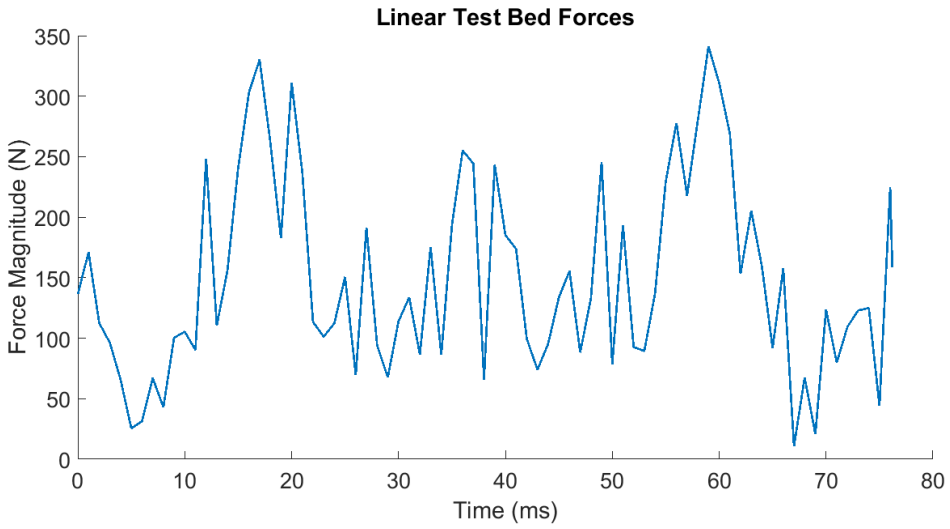

Figure 27: Magnitude of Force of Windings Spacings Simulation

With a pulley pitch diameter of 15.3 mm and a force of 350 N, the resultant torque was 2.68 Nm. For a belt speed of 1 m/s, the rotations per minute of the motor was 1248.30 RPM. A 3 mm GT2 belt was chosen for the linear test bed by reading the belt manufacture's chart on belt selection shown below in Figure 28 [46]. Timing pulleys tend to slip before breaking so the torque was the preferred load design [46].

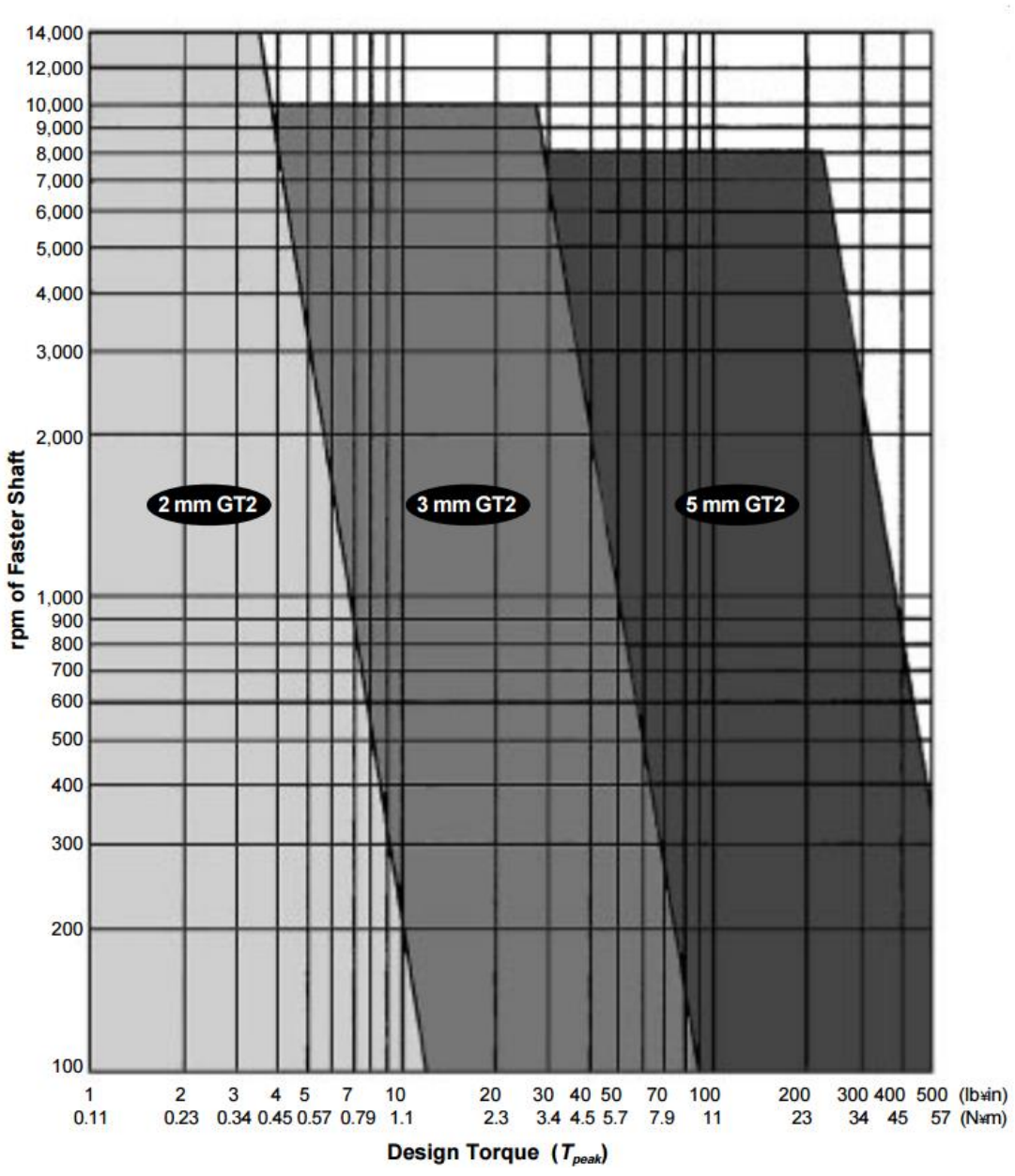

Figure 28: GT2 Belt Selection Guide [46]

For a torque of 2.68 Nm, the high torque NEMA 23 stepper motor 23HS45-4204S was selected from Stepper Online Motors & Electronics [47]. The corresponding driver M542T [48] and 350W 48V 7.3A power supply S-350-48 [49] were also purchased through Stepper Online Motors & Electronics. The stepper motor was controlled by an Arduino Mega.

3.2 Initial Linear Test Bed Testing

With the test bed built to the specifications in Appendix B, the first test was conducted similar to the windings spacing simulation from Section 2.5 above. The parameters of the experimental test are shown below in Table I.

Parameters	**Values**
Magnet to Winding Relative Linear Velocity	1/2 m/s
Number of Magnets	3
Ring Magnet Outer Diameter	3 inches
Ring Magnet Inner Diameter	2 inches
Ring Magnet Height	1/2 inch
Iron Core Diameter	1.5 inch
Coil Outer Diameter	1.505 inches
Gauge of Copper Wire	28 AWG
Measured Resistance of Copper Wire	3.8 Ω
Number of Windings	2
Windings Spacing	0.9 inches
Air Gap	1/4 inch
Length of Copper Wire, l	706.85 inches
Number of coils	150
NdFeB Grade	N42
Load Resistance	200 Ohms

Table I: Linear Test Bed Testing Parameters

Upon conducting the first test, as the magnet stack passed over the iron core, the attractive force between the core and the magnets was strong enough to bend the 3/8 inch acetal threaded rod running through the iron core keeping the stator in alignment.

All of the windings were severed as the magnet stack rubbed against the core. This was probably due to the 3D printed parts of the Linear Test Bed not being dimensionally accurate enough to keep the stator and the magnet stack concentric. It was clear that the stator needed much more rigidity to handle the attractive forces of the iron core to the magnet stack. Initially, a metal stator was avoided to remove the complexity of having a paramagnetic, conductive material as the support for the coils. However, due to the required rigidity, an aluminum stator support was essential. An updated stator design can be seen in Appendix C.

3.3 Coreless Linear Test Bed Testing

A coreless linear test bed experiment was conducted to avoid the issues with magnetic core attraction destroying stator alignment. The test involved an acetal stator support with a single winding directly wound on the rod. The parameters of the test can be seen below in Table J.

Parameters	Values
Magnet to Winding Relative Linear Velocity	1/2 m/s
Number of Magnets	3
Ring Magnet Outer Diameter	3 inches
Ring Magnet Inner Diameter	2 inches
Ring Magnet Height	1/2 inch
Acetal Core Diameter	1.5 inch
Coil Outer Diameter	1.505 inches
Gauge of Copper Wire	28 AWG
Measured Resistance of Copper Wire	1.9 Ω
Number of Windings	1
Air Gap	1/4 inch
Length of Copper Wire, l	350 inches
Number of coils	75
NdFeB Grade	N42
Load Resistance	200 Ohms

Table J: Linear Test Bed Coreless Testing Parameters

An oscilloscope was connected to the terminals of the winding to record the induced voltage in the winding. The induced voltage was then passed through a low pass filter to filter out the noise. The raw induced voltage and the filtered induced voltage can be seen for eight passes of the coil below in Figure 29 and for one pass in Figure 30.

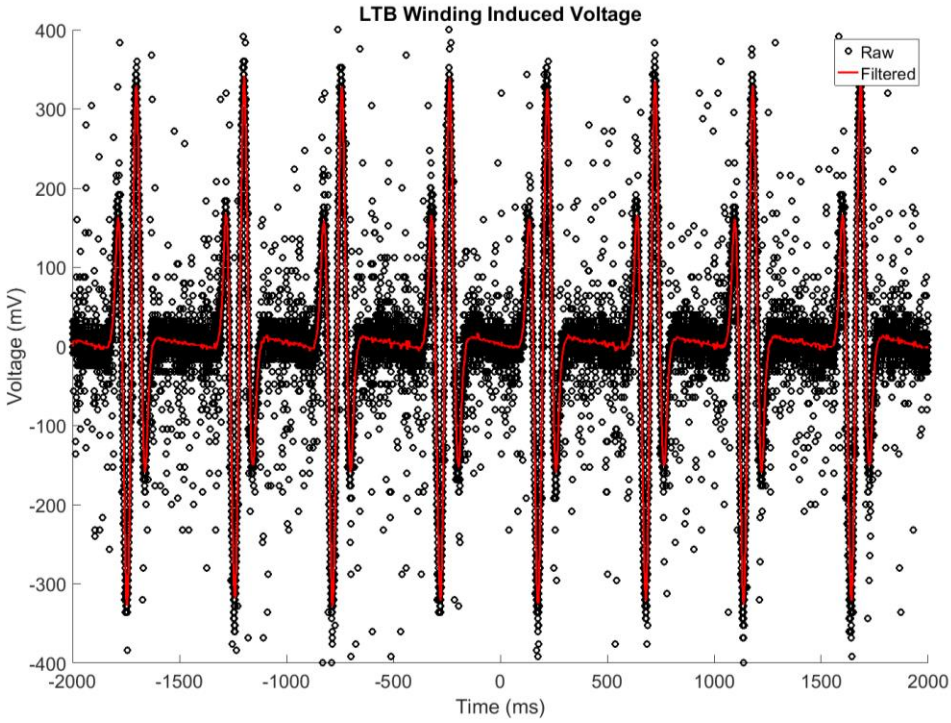

Figure 29: Experimental Induced Voltage for Eight Passes of the Winding

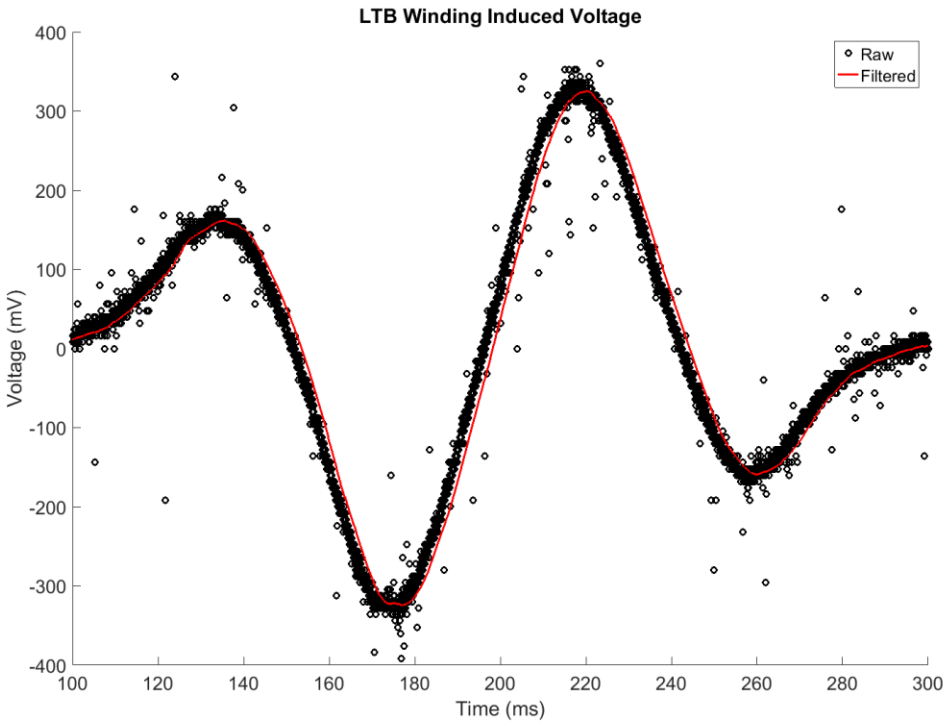

Figure 30: Experimental Induced Voltage for Eight Passes of the Winding

The peak-to-peak induced voltage is 651 mV. This test was repeated 10 times with similar results in each test.

A Maxwell simulation was created with the same parameters to provide a comparison of results. The parameters used in the Maxwell simulation can be seen in Table K below together with the starting and finishing position of the simulation in Figure 31. The light gray piece is acetal.

Parameters	Values
Magnet to Winding Relative Linear Velocity	1/2 m/s
Number of Magnets	3
Ring Magnet Outer Diameter	3 inches
Ring Magnet Inner Diameter	2 inches
Ring Magnet Height	1/2 inch
Acetal Core Diameter	1.5 inch
Coil Outer Diameter	1.505 inches
Number of Windings	1
Air Gap	1/4 inch
Length of Copper Wire, l	350 inches
Number of coils	75
NdFeB Grade	N42
Load Resistance	200 Ohms
Maxwell Step Size	1 ms

Table K: Maxwell Coreless Simulation Parameters

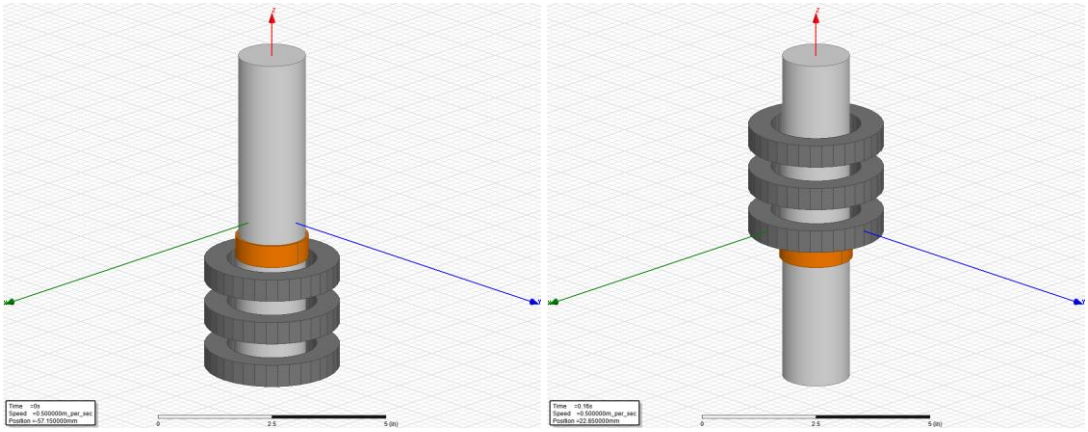

Figure 31: Starting and Finishing Positions of Coreless Maxwell Simulation

The induced voltage produce by the Maxwell simulation can be seen below in Figure 32.

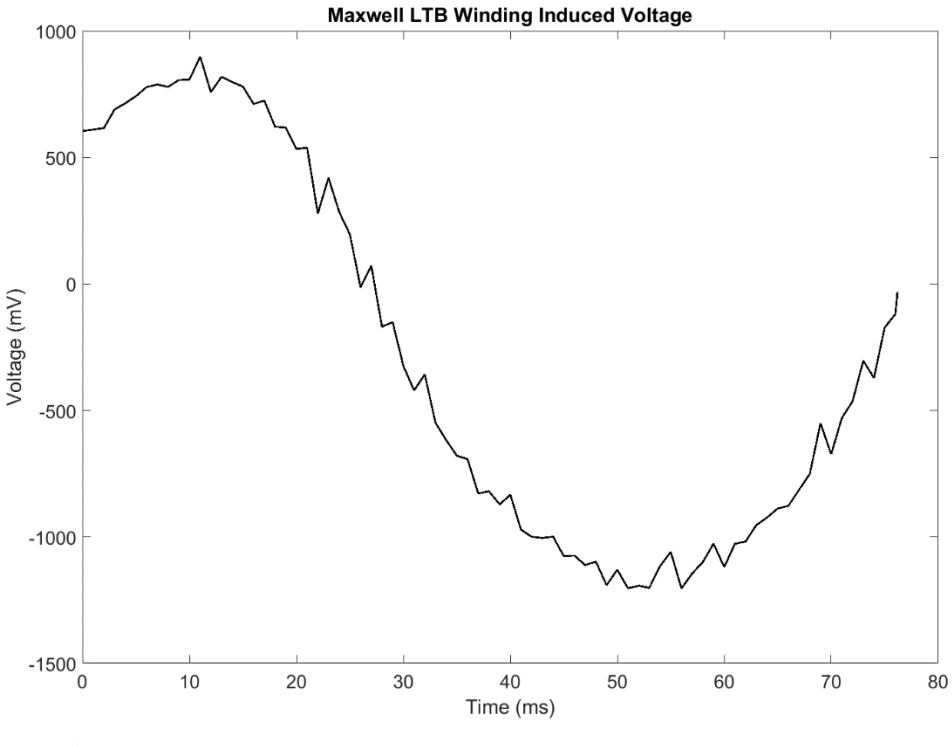

Figure 32: Coreless Maxwell Simulation Induced Voltage

The peak-to-peak voltage from the Maxwell simulation is 2 V. The experimental measured induced voltage is approximately one-third of the theoretical induced voltage from the Maxwell simulation. This could be due to interference with the magnetic field by the mildly magnetic stainless steel fasteners and the paramagnetic aluminum support used in the Linear Test Bed. With future tests, an iron core will be used to help direct and concentrate the magnetic flux towards the coils. Additionally, there were small losses in the oscilloscope and the wired connection to the winding. The winding was spooled by hand, adding a small error to the length of wire. The measured resistance value was 1.9 Ω, very close to the theoretical resistance value of 1.893 Ω for the 350 inches of 28 AWG gauge copper wire [50].

4 PMLG Final Design

The simulation presented in Section 3.5 predicts approximately a 2V peak-to-peak sinusoidal voltage at 1 m/s generator speed for a 75 coil winding corresponding to a RMS voltage of 1.4 V. The average speed of the generator used in the initial estimation model presented in Section 2.1 was 0.3384 m/s, approximately a third of the speed used in the windings spacing model in Section 2.5. From Faraday's Law, the induced voltage is directly proportional to the generator speed so the induced voltage of the same winding at 0.33 m/s corresponds to 0.47 V DC. For a 7.2 V DC output at 0.33 m/s, 16 of the 75 coils windings or 5,655 inches of magnet wire should be used. Another Maxwell simulation was performed to investigate this logic. The updated stator design with the aluminum stator support was simulated. In order to speed up the computation time, all of the 1,200 coils are assumed to be split between two windings. In practice, this would not be the case since 600 coils would not fit between the stator armature and the magnets while keeping all of the coils in a high flux region. The coils would be spread out over more windings with a larger magnet stack. This simplified approximation still captures the magnet-to-magnet interactions and the windings voltage phase but was much shorter to compute due to the decreased number of components requiring meshing. The parameters of the Maxwell simulation can be seen below in Table L.

Parameters	Values
Magnet to Winding Relative Linear Velocity	0.3384 m/s
Number of Magnets	3
Ring Magnet Outer Diameter	3 inches
Ring Magnet Inner Diameter	2 inches
Ring Magnet Height	1/2 inch
Iron Core Inner Diameter	1.25 inches
Iron Core Outer Diameter	1.5 inches
Coil Outer Diameter	1.505 inches
Aluminum Stator Support Diameter	1.25 inches
Number of Windings	2
Air Gap	1/4 inch
Length of Copper Wire, l	5,655 inches
Number of coils	1200
Windings Spacing	0.9 inches
NdFeB Grade	N42
Load Resistance	200 Ohms
Maxwell Step Size	1 ms

Table L: Final Maxwell Simulation Parameters

The starting and finishing positions for the Maxwell simulation can be seen below in Figure 33.

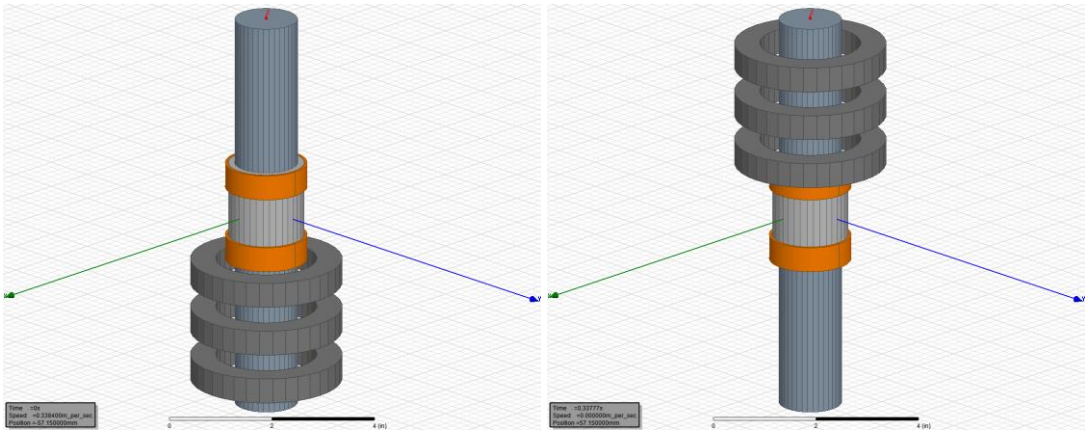

Figure 33: Final Maxwell Simulation Starting and Finishing Positions

The induced voltages in the windings can be seen below in Figure 34, together with the generated power for the windings connected in series and unconnected, independently rectified then added together in Figure 35.

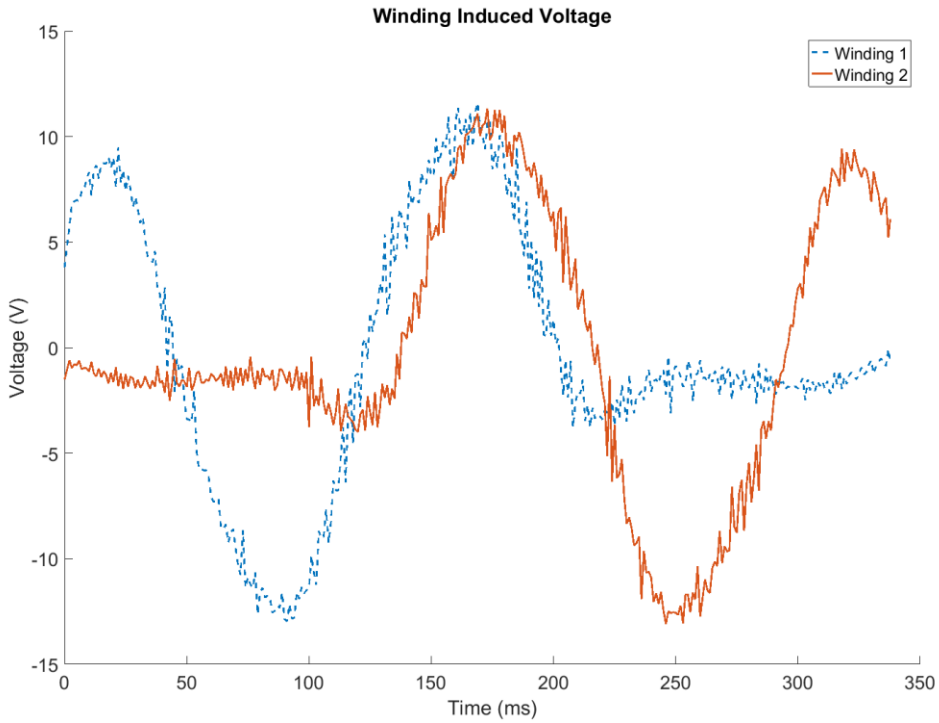

Figure 34: Maxwell Final Design Induced Voltages

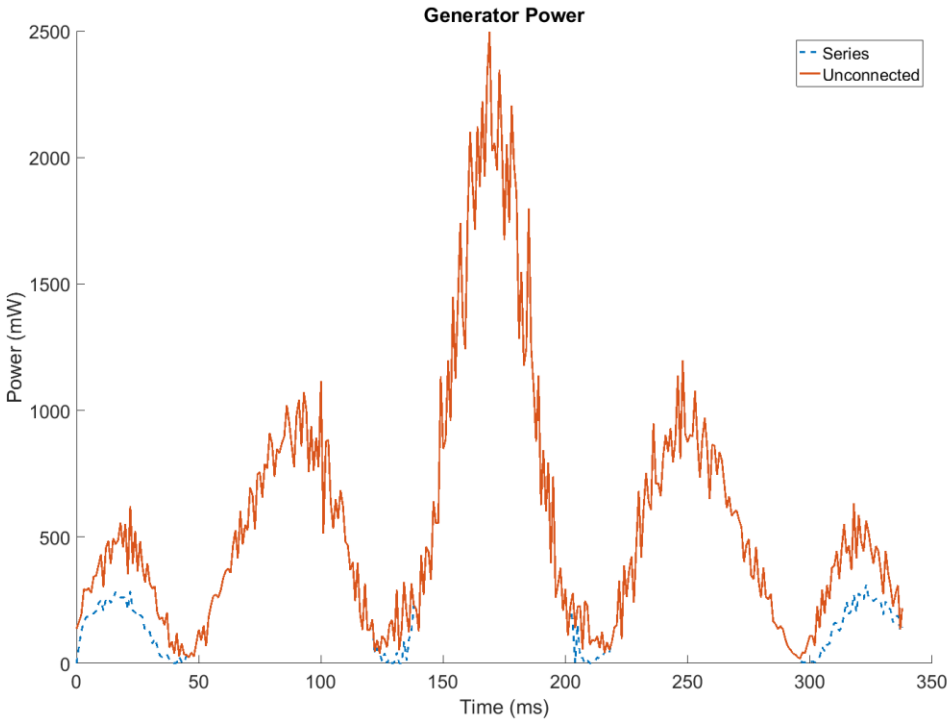

Figure 35: Maxwell Final Design Generator Power

The induced voltages are close to in-phase and have a peak to peak value of 22 V. This corresponds to a 15.56 V DC. The average power for the windings connected in series is 517.93 mW while the unconnected windings that would need to be rectified individually are 570.50 mW. This is a close enough difference to warrant connecting in series to avoid complications in rectification. The current for the windings connected in series is shown below in Figure 36.

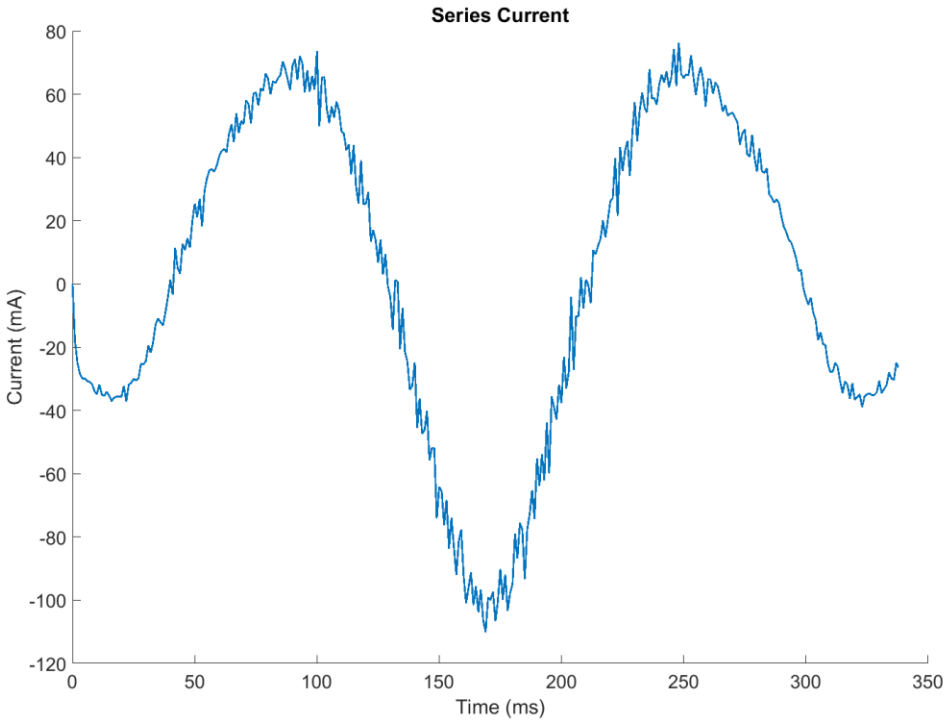

Figure 36: Maxwell Final Design Series Current

The series current has a peak to peak value of 180 mA. The resulting forces required to move the magnets over the windings can be seen in Figure 37 below.

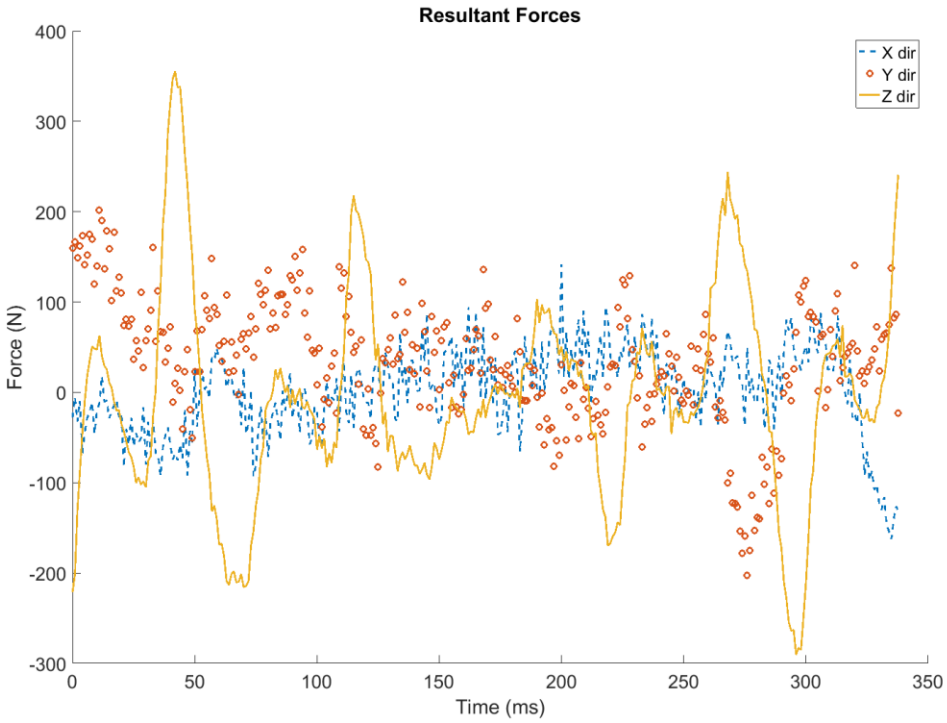

Figure 37: Maxwell Final Resultant Forces

With a maximum force in the z-direction (the linear direction) of 355 N, the drag platform must be 3.18 square meters. The average magnitude of the force in the z-direction is 81.09 N corresponding to a drag platform of 0.725 square meters.

The above design would provide enough power for the average speed of a typical generator attached to a chipod. The generator provides 512 mW of average power. This will allow for the inefficiencies associated with the electronic circuits used to rectify the power, store the power, and use a DC/DC voltage converter to produce a constant 7.2 V voltage for the chipod.

5 DC/DC Voltage Converter

The ending power condition of 250 mW at 7.2 V DC to power the chipod is known. Originally, the customer requirement for the chipod constant voltage was specified to be 5V at 250 mW. This customer requirement was changed by the customer to be 7.2 V at 250 mW. The electrical circuit described below was for the original customer requirement of 5V, but by following the process outlined below it could be updated to fit the new customer requirement.

Working backwards from the chipod, the circuitry required to filter the power produced by the generator was determined. Since the chipod requires a low power DC input and the Permanent Magnet Linear Generator (PMLG) does not interface to the grid at all, a single-phase generator could be used instead of a three-phase generator. The block diagram of the electrical circuit required to filter the power output of the generator can be seen below in Figure 38.

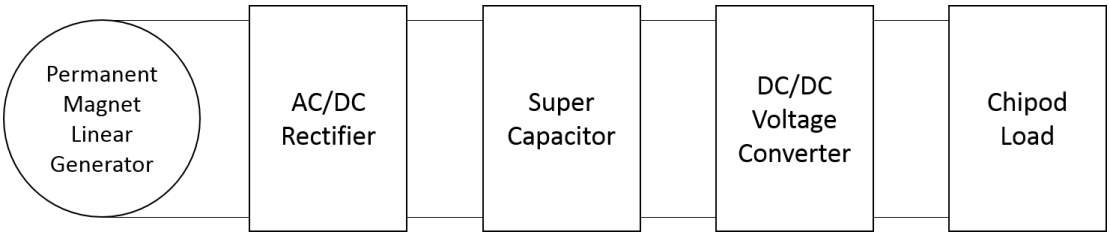

Figure 38: Circuit Block Diagram Schematic

For the AC/DC rectifier, a simple full bridge diode rectifier was used--specifically a Fairchild DF005M Bridge Rectifier [51]. The circuit diagram for a full bridge rectifier can be seen below in Figure 39, together with the voltage and current waveforms detailing the rectification [52].

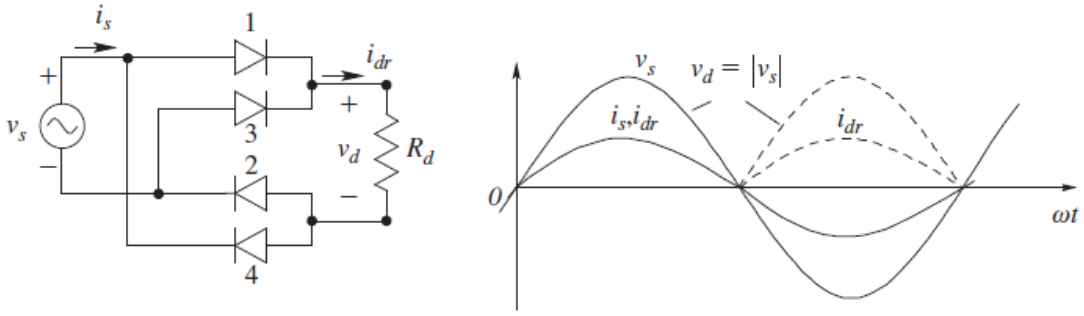

Figure 39: Full Bridge Rectifier [52]

A voltage converter is necessary to increase the efficiency and allow for the discontinuous nature in many renewable energy sources. Interleaved boost converters are a good option for low power renewable energy applications, due to the high voltage step up and high efficiency [53] [54]. A Simulink model of the interleaved boost converter for this application can be seen below in Figure 40. Table M contains the parameters used for the interleaved converter.

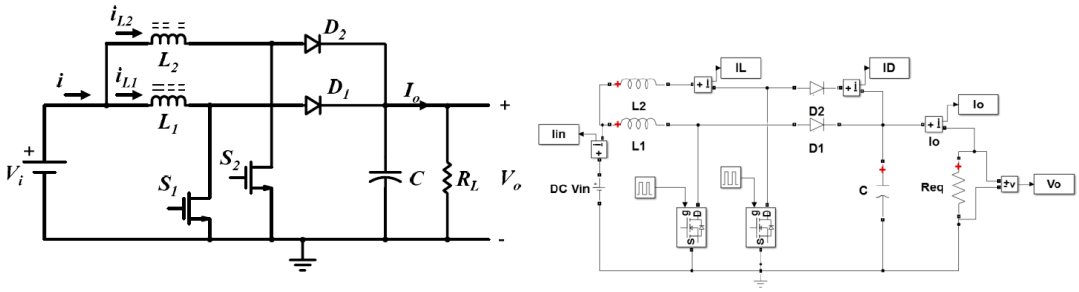

Figure 40: Interleaved Boost Converter Circuit Diagram and Simulink Simulation

Parameters	Value
AC Voltage source	3.35 V
Rectifier Capacitor, C1	10 µF
DC Voltage Input, Vin	1.75 V
Inductors, L1 and L2	1 mH
Interleaved Boost Converter Capacitor, C	0.1 mF
Load Resistor, Req	100 Ω
MOSFETs Duty Ratio	70%
Switching Frequency, fs	10 kHz

Table M: Interleaved Boost Converter Component Values

From the Simulink model, waveforms of the input voltage, input current, diode current, inductor current, output voltage and output current were obtained. These waveforms can be seen in Figures 41-47 below.

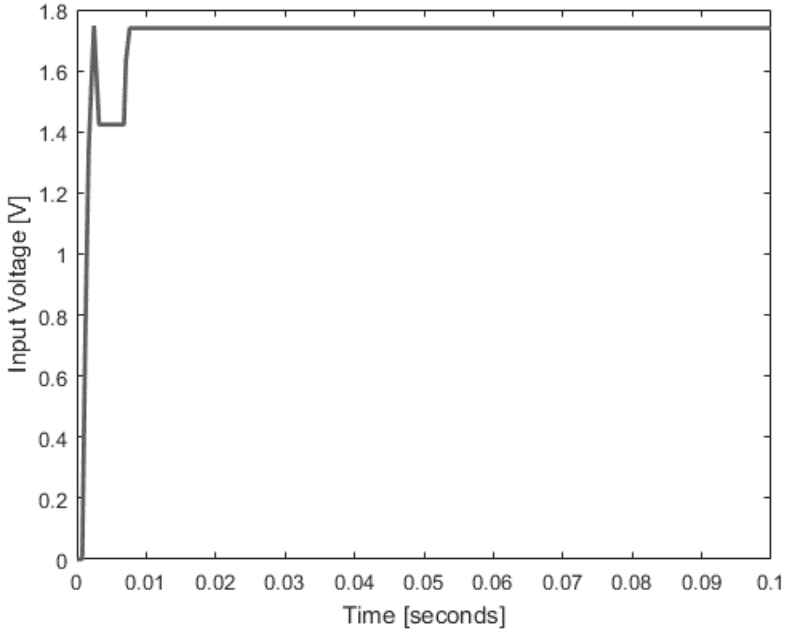

Figure 41: Interleaved Boost Converter Input Voltage

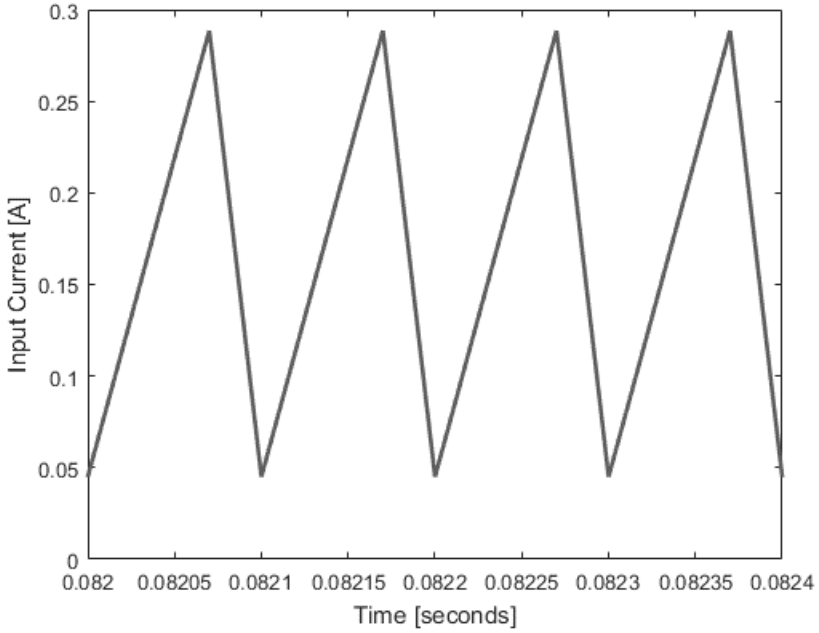

Figure 42: Interleaved Boost Converter Input Current

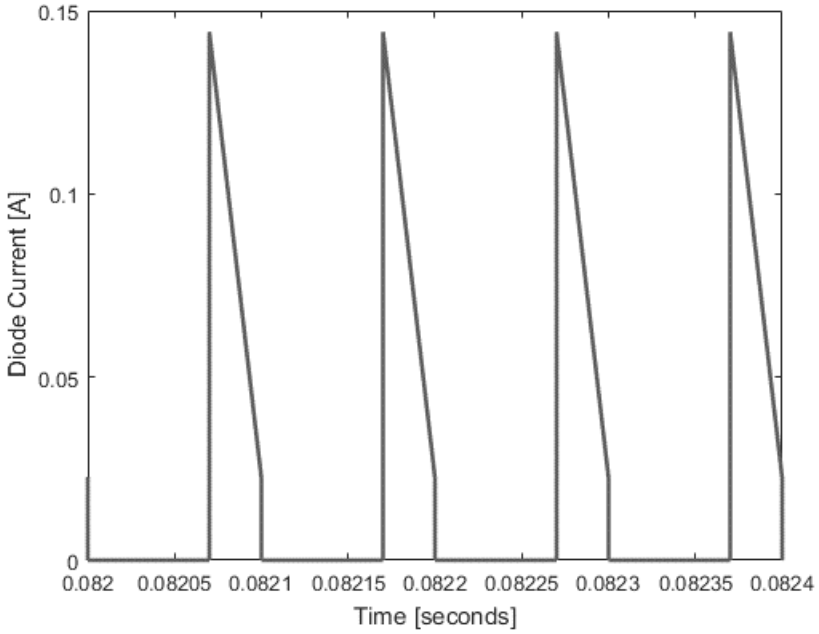

Figure 43: Interleaved Boost Converter Diode Current

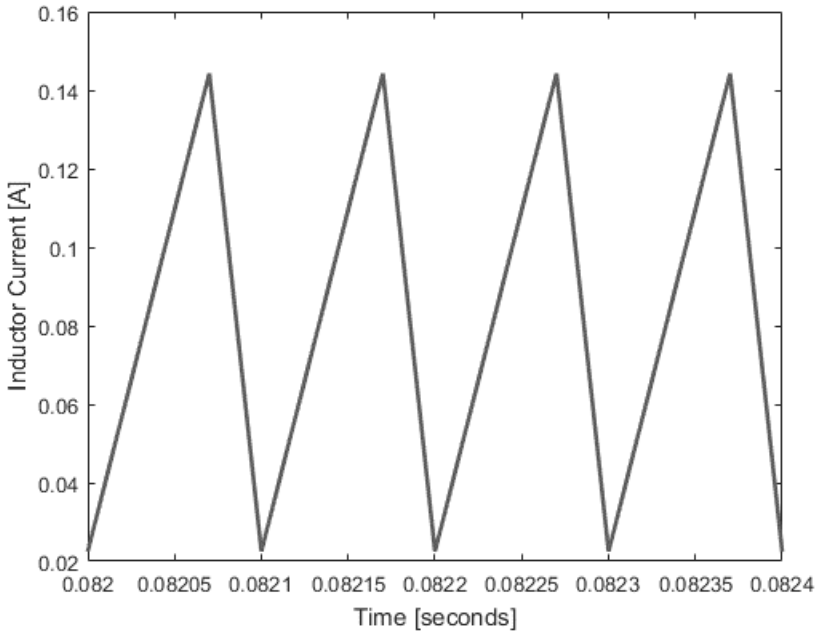

Figure 44: Interleaved Boost Converter Inductor Current

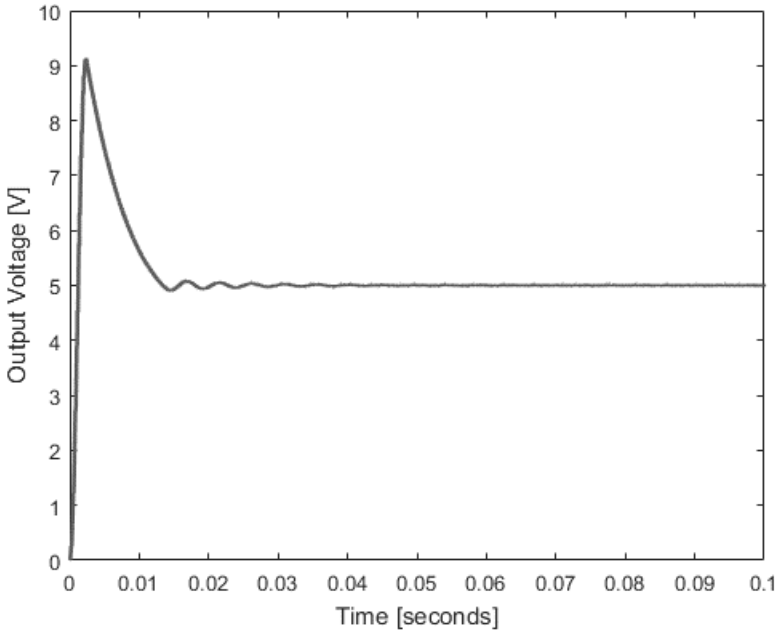

Figure 45: Interleaved Boost Converter Output Voltage

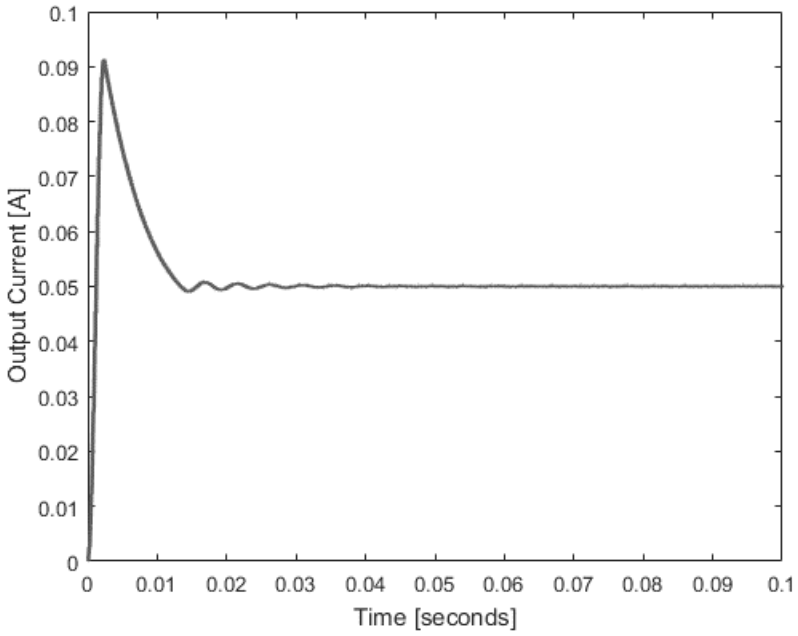

Figure 46: Interleaved Boost Converter Output Current

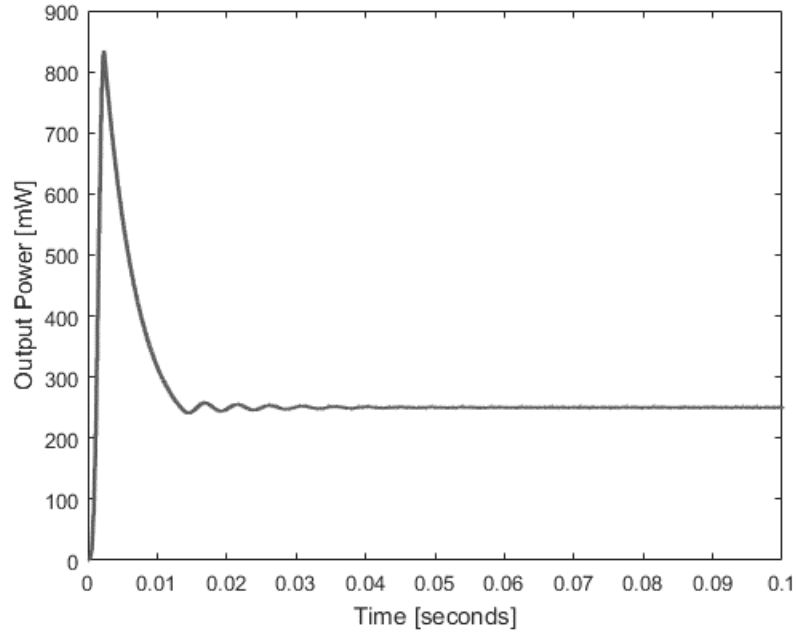

Figure 47: Interleaved Boost Converter Output Power

The resulting power characteristics of the interleaved boost converter can be seen below in Table N.

Parameters	Value
DC Voltage Source, Vin	1.75 V
Mean Input Current	0.178 A
Mean Input Power, Pin	312 mW
Voltage Output, Vo	5.0 V
Current Output, Io	0.05 A
Power Output, Po	250 mW

Table N: Power Characteristics for the Interleaved Boost Converter

The efficiency of this interleaved boost converter is 80.13%. Further optimization of the MOSFET switching frequencies and components used should be performed to ensure this interleaved circuit is highly efficient. In practice, tuning the separate MOSFETs to switch perfectly in sync with each other proved to be problematic. Due to the difficulties building the interleaved boost converter, a commercially available buck boost converter was a better option for this application and project timeline.

The advantages of the buck-boost voltage regulators are that they can provide constant voltage output regardless of whether the input source is at a higher or lower voltage. A Linear Technology 15V, 200mA Synchronous Buck-Boost DC/DC Converter LTC3129-1 was chosen for this application [55]. The circuit diagram for this buck-boost converter can be seen below in Figure 48, courtesy of Linear Technology [55].

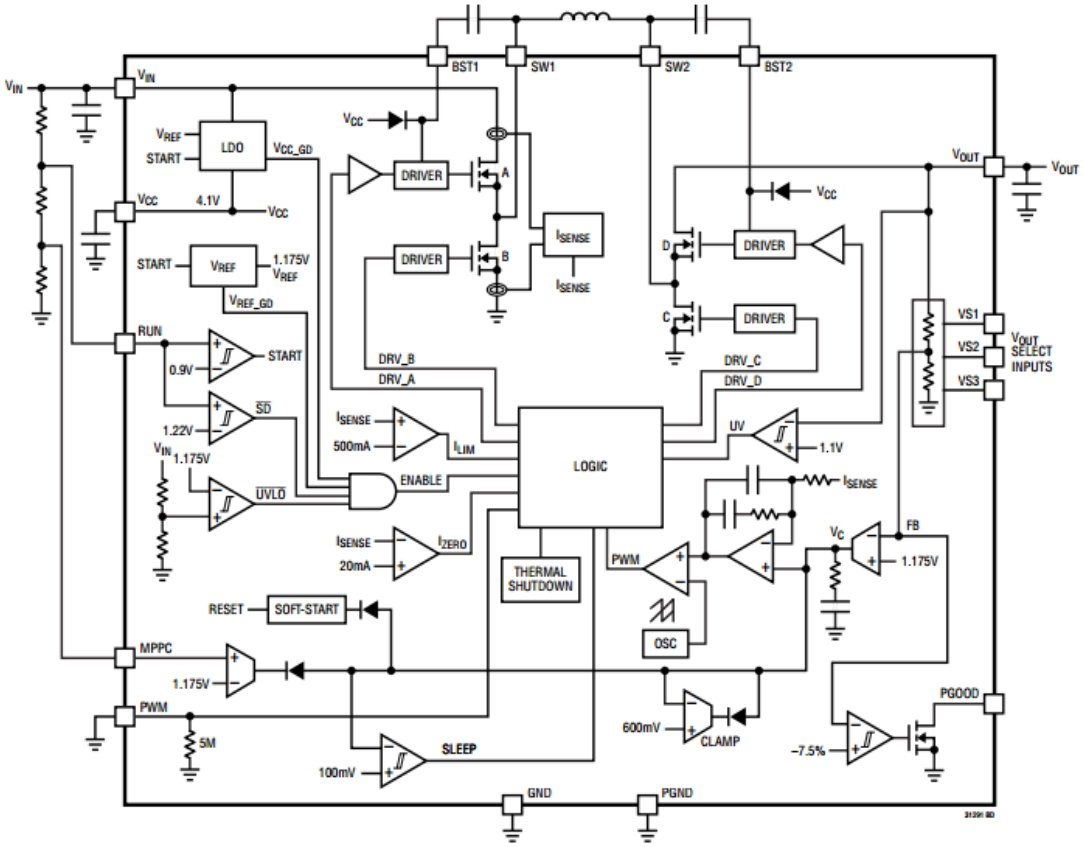

Figure 48: LTC3129-1 Buck-Boost Converter [55]

Linear Technology additionally sells demo boards with the LTC3129 microchip installed and all of the needed filtering external capacitors and resistors attached. This board was purchased and, with the help of Linear Technology, an LTSpice simulation [55] was made. This LTSpice model can be seen below in Figure 49.

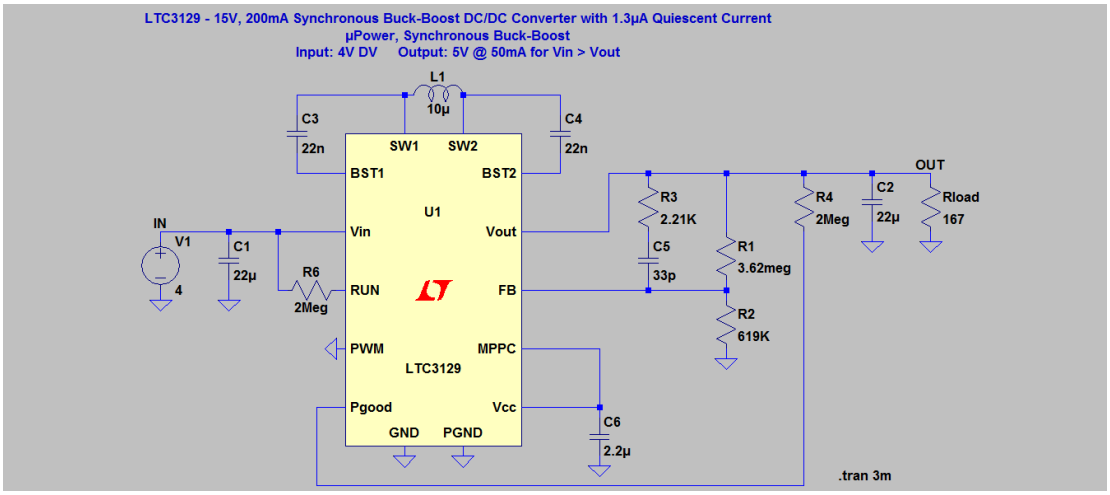

Figure 49: DC Input Circuit Model for the Buck Boost Converter

The current demo board does not have the capability to output 7.2 V but the microchip could be purchased separately and by changing the value of the R1 resistor, 7.2 V can be achieved. The input and output voltage, current, and power waveforms of the current DC LTSpice model can be seen below in Figures 50-51.

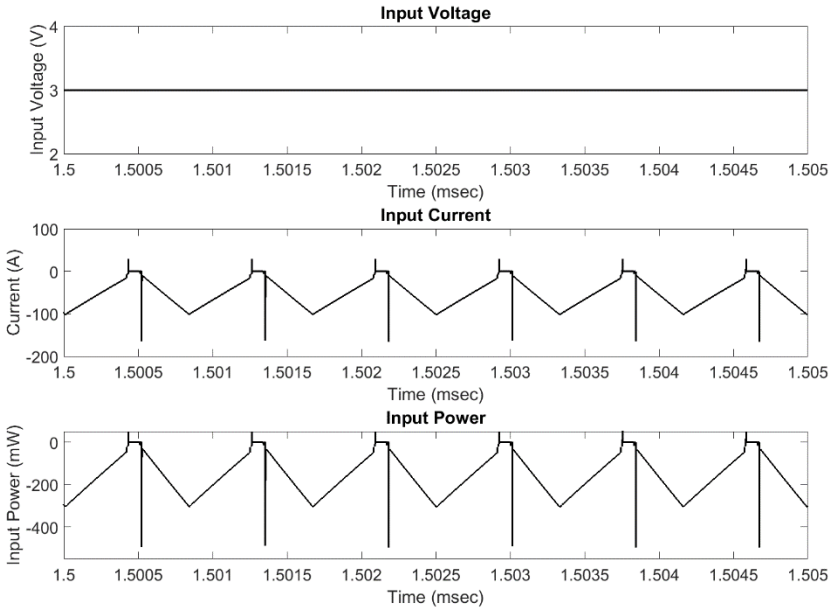

Figure 50: Input Waveforms to Buck-Boost Converter

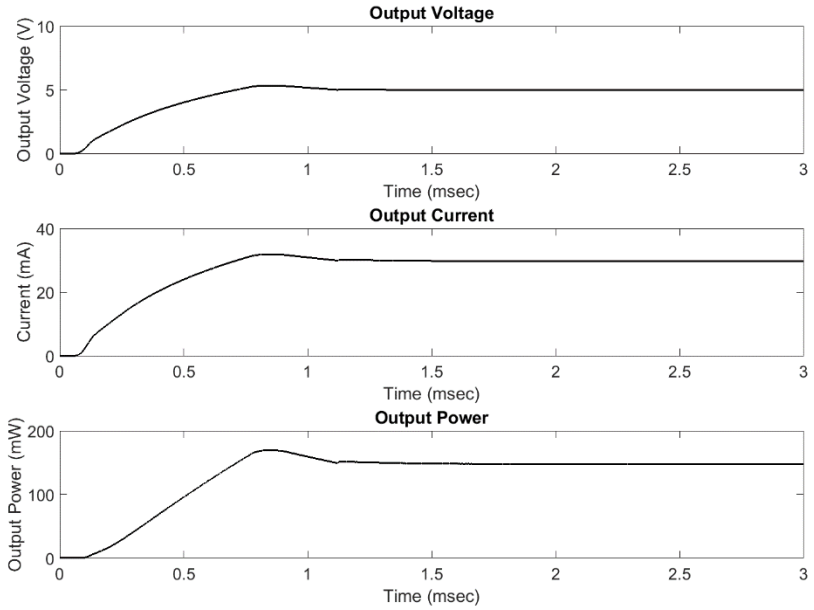

Figure 51: Output Waveforms from the Buck-Boost Converter

The power characteristics for this buck boost converter are shown below in Table O.

Parameters	Value
AC Voltage Source, Vin	4V
Mean Input Current	77 mA
Mean Input Power, Pin	230 mW
Voltage Output, Vo	5.0 V
Current Output, Io	30 mA
Power Output, Po	150 mW

Table O: Power Characteristics for the Buck-Boost Converter

The efficiency of this buck-boost converter under these operating conditions is 65.22%. The efficiency increases as the input voltage increases. The manufacturer's efficiency curves for the buck-boost demo board can be seen below in Figure 52 [55].

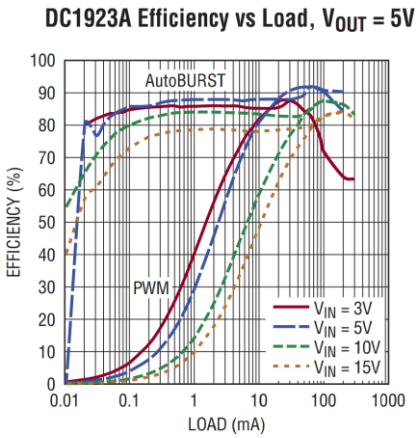

Figure 52: Efficiency Curves for the Buck-Boost Converter [55]

The low operating efficiency at low input voltages highlights why the interleaved boost converter described above would be beneficial to contract out to an electrical engineer.

The above LTSpice model could be updated to include the final generator modelled as a sinusoidal AC voltage source, as shown in Figure 53 below.

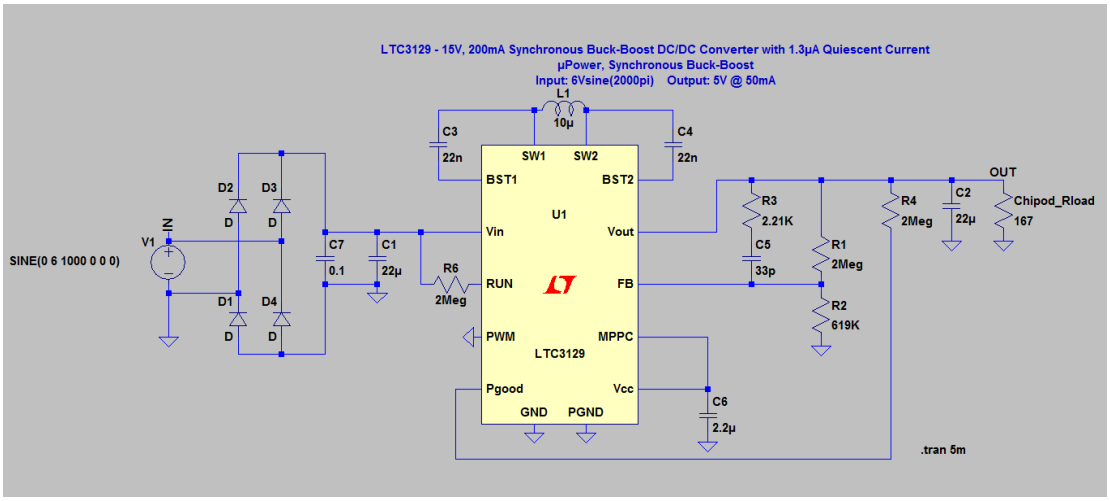

Figure 53: Electrical Circuit Model for the PMLG

The ultimate value of the super capacitor needed for the updated voltage could be found by increasing the value of the capacitor C7 (currently 0.1F) in the LTSpice model until a constant DC output is reach. This would be repeated experimentally for

capacitors around the same magnitude as the theoretical capacitance found in the LTSpice model.

6. Discussions and Conclusions

The initial model for the PMLG using Faraday's Law and Lorentz's Law does not properly account for the changing magnetic field and flux lines. The more advanced Maxwell simulations are required to properly model a PMLG. At this point in the project, the theoretical design of the PMLG for a constant generator speed of 0.3384 m/s, the average generator velocity based on chipod data and an assumed stroke limit of 400 mm, was presented in Section 3.4. The final design can be scaled based on the results of further linear test bed experiments.

The linear test bed has been designed and manufactured. Now, further tests need to be conducted with the iron core to confirm the findings of the Maxwell simulation. There will be some error associated between the experimental data and the Maxwell simulation due to the Maxwell simulation being the ideal case. The current experiments performed did not have an iron core. This potentially increased the error between the Maxwell simulation and the experimental tests. The linear test bed is not contained in a vacuum like the Maxwell simulation so there were external objects interfering with the magnetic field such as the stepper motor, mildly magnetic fasteners, and paramagnetic aluminum extrusion frame. Having the iron core in the tests will increase the flux around the coils and reduce the effect of the surrounding objects.

During the linear test bed experiments, noise in the measured induced voltage was observed when the power supply was turned on. The magnet stack can be actuated by hand. When the magnet stack was driven by hand, very low noise in the induced voltage was measured. As soon as the power supply was turned on, the noise level drastically increased, even when the stepper motor was not engaged. It is unclear what could be causing this but it may be due to high frequency vibrations from the power supply or improper grounding. Attempts were made to ensure grounding of the electronics and isolation of power supply and linear test bed but these attempts had no

effect on the noise level. A low pass filter did well to filter out the noise from the measured data.

The linear test bed could be improved by including an accelerometer to measure velocity. Currently, the speed of the test bed is calculated from the stepper motor's stepping speed and the pulses per revolution. This does not take into account whether the timing belt is slipping at all due to the variable forces as the magnet stack passes over the coils.

The next step for the theoretical simulations will be updating the Maxwell simulation to account for the semi-sinusoidal irregular velocity induced by the ocean waves. No attempt has been made to waterproof or pressure case the mechanical system. All of the Maxwell simulations conducted assumed an air gap of ¼ inch. This is a relatively large air gap for permanent magnet linear generators but this assumption was made due to the necessity to waterproof and pressure case the design. The Maxwell simulation should be updated geometrically as the mechanical system is designed.

The chipod time varying RLC characteristics are unknown. Defining this would be helpful to further simulate the electrical circuit. The commercially available DC/DC voltage converter from Linear Technology can be used to provide constant voltage to the chipod. However, manufacturing an interleaved boost converter may increase the efficiency of the circuit.

Renewable energy sources are becoming increasingly important due to their low environmental impact and limitless nature. While many wave energy converters exist, this is a unique application because the wave energy device is neither at the surface nor at the seafloor and is a low power application. The permanent magnet linear generator described above would enable the continuous operation of ocean mixing sensors with minimal maintenance.

Bibliography

[1] J. Andrews and N. Jelley, Energy Science: Principles, Technologies, and Impacts, Oxford: Oxford University Press, 2013.

[2] K. Koca, A. Kortenhaus, H. Oumeraci, B. Zanuttigh, E. Angelelli, M. Cantu, R. Suffredini and G. Franceschi, "Recent Advances in the Development of Wave Energy Converters," in *European Wave and Tidal Energy Conference*, Aalborg, 2013.

[3] J. H. Prudell, "Novel Design and Implementation of a Permanent Magnet Linear Tubular Generator for Ocean Wave Energy Conversion," Oregon State University Electrical and Computer Engineering, Corvallis, 2007.

[4] J. Prudell, M. Stoddard, E. Amon, T. K. A. Brekken and A. v. Jouanne, "A Permanent-Magnet Tubular Linear Generator for Ocean Wave Energy Conversion," *IEEE Transactions on Industry Applications,* vol. 46, no. 6, pp. 2392-2400, 2010.

[5] D. A. Gemme, S. P. Bastien, R. B. Sepe, J. Montgomery, S. T. Grilli and A. Grilli, "Experimental Testing and Model Validation for Ocean Wave Energy Harvesting Buoys," in *Energy Conversion Congress and Exposition (ECCE)*, Denver, 2013.

[6] S. P. Bastien, R. B. Sepe, A. R. Grilli, S. T. Grilli and M. L. Spaulding, "Ocean Wave Energy Harvesting Buoy for Sensors," in *Energy Conversion Congress and Exposition*, San Jose, 2009.

[7] Ocean Power Technologies Inc., "Powerbuoy Technology," [Online]. Available: http://www.oceanpowertechnologies.com/powerbuoy-technology/. [Accessed 22 January 2016].

[8] T. Lettenmaier, A. von Jouanne, E. Amon, S. Moran and A. Gardiner, "Testing the WET-NZ Wave Energy Converter Using the Ocean Sentinel Instrumentation Buoy," *Marine Technology Society Journal,* vol. 47, no. 4, pp. 164-176, 2013.

[9] A. Weinstein, G. Fredrikson, M. Parks and K. Neislen, "AquaBuOY – The Offshore Wave Energy Converter: Numerical Modeling and Optimization," in *Ocean Energy Conference*, Kobe, 2004.

[10] J. Weber, F. Mouwen, A. Parish and D. Robertson, "Wavebob – Research & Development Network and Tools in the Context of Systems Engineering," in *European Wave and Tidal Energy Conference*, Uppsala, 2009.

[11] T. Brekken, K. Rhinefrank, A. v. Jouanne, A. Schacher, J. Prudell and E. Hammagren, "Scaled Development of a Novel Wave Energy Converter Including Numerical Analysis and High-Resolution Tank Testing," *Proceedings of the IEEE,* vol. 101, no. 4, pp. 866-875, 2013.

[12] K. Rhinefrank, A. Schacher, J. Prudell, E. Hammagren, A. v. Jouanne and T. Brekken, "Scaled development of a novel Wave Energy Converter through wave tank to utility-scale laboratory testing," in *Power & Energy Society General Meeting*, Denver, 2015.

[13] L. Margheritini, "Wave Energy, Lever Operated Pivoting Float LOPF Study," Aalborg University, Aalborg, 2011.

[14] R. H. Hansen, M. M. Kramer and E. Vidal, "Discrete Displacement Hydraulic Power Take-Off System for the Wavestar Wave Energy Converter," *Energies,* vol. 6, pp. 4001-4044, 2013.

[15] Seabased AB, "Seabased Wave Technology," Seabased AB, [Online]. Available: http://www.seabased.com/en/technology/seabased-wave-energy. [Accessed 22 January 2016].

[16] R. Henderson, "Design, Simulation, and Testing of a Novel Hydraulic Power Take-Off System for the Pelamis Wave Energy Converter," *Renewable Energy,* vol. 31, no. 2, pp. 271-283, 2006.

[17] G. Dalton, R. Alcorn and T. Lewis, "Case study feasibility analysis of the Pelamis wave energy convertor in Ireland, Portugal and North America," *Renewable Energy,* vol. 35, no. 2, pp. 443-455, 2010.

[18] J. P. Kofoed, "Hydraulic evaluation of the DEXA wave energy converter," Department of Civil Engineering, Aalborg University, Aalborg, 2009.

[19] L. Cameron, R. Doherty, A. Henry, K. Doherty, J. V. Hoff, D. Kaye, D. Naylor, S. Bourdier and

T. Whittaker., "Design of the Next Generation of the Oyster Wave Energy Converter," in *International Conference on Ocean Energy*, Bilbao, 2010.

[20] BioPower Systems Pty. Ltd, "bioWAVE," [Online]. Available: http://bps.energy/biowave. [Accessed 22 January 2016].

[21] E. Ramudu, "Ocean Wave Energy-Driven Desalination Systems for Off-Grid Coastal Communities in Developing Countries," in *IEEE Global Humanitarian Technology Conference*, Seattle, 2011.

[22] J. Lucas, M. Livingstone, M. Vuorinen and J. Cruz, "Development of a Wave Energy Converter (WEC) Design Tool – Application to the WaveRoller WEC Including Validation of Numerical Estimates," in *International Conference on Ocean Energy*, Dublin, 2012.

[23] The Engineering Business Ltd, "Frond Wave Energy Converter Phase 2," Crown Copyright, 2005, 2005.

[24] A. Pecher, J. Kofoed, l. J. Espeda and S. Hagberg, "Results of an Experimental Study of the Langlee Wave Energy Converter.," in *International Offshore and Polar Engineering Conference*, Beijing, 2010.

[25] B. C. Boren, B. A. Batten and R. K. Paasch, "Active Control of a Vertical Axis Pendulum Wave Energy Converter," in *American Control Conference* , Portland, 2014.

[26] Wello Oy, "The Penguin Wave Energy Converter," Wello Direct Conversion, [Online]. Available: http://www.wello.eu/en/penguin. [Accessed 23 January 2016].

[27] J. P. Kofoeda, P. Frigaarda, E. Friis-Madsenb and H. C. Sørensenc, "Prototype Testing of the Wave Energy Converter Wave Dragon," *Renewable Energy,* vol. 31, no. 2, pp. 181-189, 2006.

[28] Rasmussen and Skaarup, "Working principles of the WavePlane," in *European Wave Energy Conference*, Aalborg, 2000.

[29] A. F. Falcão and J. C. Henriques, "Oscillating-water-column wave energy converters and air turbines: A review," *Renewable Energy,* vol. 85, pp. 1391-1424, 2016.

[30] T. Heath, T. Whittaker and C. Boake, "The Design, Construction and Operation of the LIMPET Wave Energy Converter," in *European Wave Energy Conference*, Aalborg, 2000.

[31] Oceanlinx, "Oceanlinx Technology greenWAVE," [Online]. Available: http://www.oceanlinx.com/technology/products/greenwave. [Accessed 23 January 2016].

[32] Oceanlinx, "Oceanlinx Technology ogWAVE," [Online]. Available: http://www.oceanlinx.com/technology/products/ogwave-2. [Accessed 23 January 2016].

[33] Oceanlinx, "Oceanlinx Technology blueWAVE," [Online]. Available: http://www.oceanlinx.com/technology/products/bluewave. [Accessed 23 January 2016].

[34] H. Polinder, M. E. Damen, F. Gardner and M. G. d. S. Prado, "Archimedes Wave Swing Linear Permanent-Magnet Generator System Performance," in *European Wave and Tidal Energy Conference*, Glasgow, 2005.

[35] AWS Ocean Energy Ltd, "Archimedes Waveswing Submerged Wave Power Buoy," Weebly, [Online]. Available: http://www.awsocean.com/archimedes-waveswing.html. [Accessed 25 January 2016].

[36] M. G. Hughes and A. D. Heap, "National-Scale Wave Energy Resource Assessment for Australia," *Renewable Energy,* vol. 35, no. 8, pp. 1783-1791, 2010.

[37] Carnegie Wave Energy Limited, "Carnegie Clean Energy: What is CETO," [Online]. Available: http://carnegiewave.com/what-is-ceto/. [Accessed 25 January 2016].

[38] M. Stieber, "Design of a Small Scale Power Generation Device for Undersea Moored Sensor Arrays," Oregon State University Mechanical Engineering, Corvallis, 2015.

[39] H. Polinder, M. Mueller, M. Scuotto and M. G. d. S. Prado, "Linear Generator Systems for Wave Energy Conversion," in *European Wave and Tidal Energy Conference*, Porto, 2007.

[40] H. Polinder, B. Mecrow, A. Jack, P. Dickinson and M. Mueller, "Linear Generators for Direct-

Drive Wave Energy Conversion," in *Electric Machines and Drives Conference*, Madison, 2003.

[41] B. Munson, D. Young, T. Okiishi and W. Huebsch, Fundamentals of Fluid Mechanics, John Wiley & Sons, Inc., 2009.

[42] K&J Magnetics, Inc., "RZ0Y0X0," [Online]. Available: https://www.kjmagnetics.com/proddetail.asp?prod=RZ0Y0X0. [Accessed 20 May 2017].

[43] A. Taflove and S. C. Hagness, Computational electrodynamics : The Finite-Difference Time-Domain Method, Boston: Artech House, 2005.

[44] Applied Magnets, "Applied Magnets Neodymium Ring Magnets 3 in OD x 2 in ID x 1/2 in Rare Earth N42," [Online]. Available: http://appliedmagnets.com/neodymium-ring-magnets-3-in-od-x-2-in-id-x-1-2-in-rare-earth-n42-p-663.html. [Accessed 24 5 2017].

[45] Designatronics Inc., "A 6A53M016DF0606," Stock Drive Products/Sterling Instrument , [Online]. Available: http://shop.sdp-si.com/catalog/product/?id=A_6A53M016DF0606. [Accessed 24 May 2017].

[46] Designatronics Inc., "Timing Belt Drive Selection Procedure," Stock Drive Products / Sterling Instrument, [Online]. Available: http://www.sdp-si.com/D265/PDF/D265T146.pdf. [Accessed 24 5 2017].

[47] Stepper Online Motors & Electronics, "High Torque Nema 23 CNC Stepper Motor 113mm 3Nm(425oz.in) 23HS45-4204S," [Online]. Available: http://www.omc-stepperonline.com/high-torque-nema-23-cnc-stepper-motor-113mm-3nm425ozin-23hs454204s-p-127.html. [Accessed 24 May 2017].

[48] Stepper Online Motors & Electronics, "2/4 phase Nema 23 Stepper Motor Driver 24-50VDC 1.5A-4.5A 256 Microstep M542T," [Online]. Available: http://www.omc-stepperonline.com/24-phase-nema-23-stepper-motor-driver-2450vdc-15a45a-256-microstep-m542t-p-293.html. [Accessed 24 May 2017].

[49] Stepper Online Motors & Electronics, "Switching Power Supply 350W 48V 7.3A for CNC Router Kits 115V/230V S-350-48," [Online]. Available: http://www.omc-stepperonline.com/switching-power-supply-350w-48v-73a-for-cnc-router-kits-115v230v-s35048-p-158.html. [Accessed 24 May 2017].

[50] Cirris Systems, "Wire Resistance Calculator & Table," [Online]. Available: https://www.cirris.com/learning-center/calculators/133-wire-resistance-calculator-table. [Accessed 25 May 2017].

[51] Semiconductor Components Industries LLC, "DF005M-DF10M Bridge Rectifiers," Fairchild, [Online]. Available: https://www.fairchildsemi.com/datasheets/DF/DF005M.pdf. [Accessed 30 January 2017].

[52] N. Mohan, Power Electronics: A First Course, Hoboken: John Wiley & Sons, Inc., 2012.

[53] A. J. Rahavi, T. Kanagapriya and R. Seyezhai, "Design and Analysis of Interleaved Boost Converter for Renewable Energy Source," in *International Conference on Computing, Electronics and Electrical Technologies*, Tamil Nadu, 2012.

[54] N. Smith and R. McCann, "Analysis and Simulation of a Multiple Input Interleaved Boost Converter for Renewable Energy Applications," in *Telecommunications Energy Conference (INTELEC)*, Vancouver, 2014.

[55] Linear Technology, "LTC3129-1 - 15V, 200mA Synchronous Buck-Boost DC/DC Converter with 1.3μA Quiescent Current," [Online]. Available: http://www.linear.com/product/LTC3129-1. [Accessed 15 November 2016].

Appendix A. PMLG First Approximation MATLAB Script

```
%% Generator initialization file
clc
clear
format compact
close all

%% Parameters

L = 120; %m
B = 0.25; %T
R_load = 206; %Ohms
d = 0.0105; %m
stroke = 0.4; %m


%% Load water surface elevation time series
load('C:\Users\Lillian\Box Sync\Thesis\thesis folder lab
computer\Generator
Simulation\chipodvelocitydata\avg_chi_20150323T040000.mat', 'avg')
t = [0:length(avg.velz)-1];
t = t';
u_timeseries = [t avg.velz']; %m/s

t = [0:length(avg.dispz)-1];
t = t';
z_timeseries = [t avg.dispz'];

for i = 1:1:7200
    if abs(z_timeseries(i,2)) > stroke/2
        u_timeseries(i,2) = 0;
    end
end

%% Constant Amplitude Sine Velocity
% t1 = 0:0.1:720;
% u_y = 0.4*sin(2*pi*0.3*t1);
% t1 = [0:length(u_y)-1];
% u_timeseries = [t1' u_y']; %m/s

%% Call Simulink
sim('gensim')

%% Results
figure(1)
hold on
subplot(2,1,1)
plot(z_timeseries(:,1), z_timeseries(:,2))
xlabel('time (sec)')
ylabel('Displacement_z (m)')
xlim([0 100])
```

```
subplot(2,1,2)
plot(u_timeseries(:,1), u_timeseries(:,2))
xlabel('time (sec)')
ylabel('Velocity_z (m/s)')
xlim([0 100])

figure(2)
hold on
subplot(3,1,1)
plot(P.time, P.data)
xlabel('time (sec)')
ylabel('Power (W)')
xlim([0 100])
ylim([-1 5])
subplot(3,1,2)
plot(I.time, I.data)
xlabel('time (sec)')
ylabel('Current (A)')
xlim([0 100])
subplot(3,1,3)
plot(V.time, V.data)
xlabel('time (sec)')
ylabel('Voltage (V)')
xlim([0 100])

disp('The number of windings is')
disp(mean(N))
```

Appendix B. Linear Test Bed SolidWorks Drawings

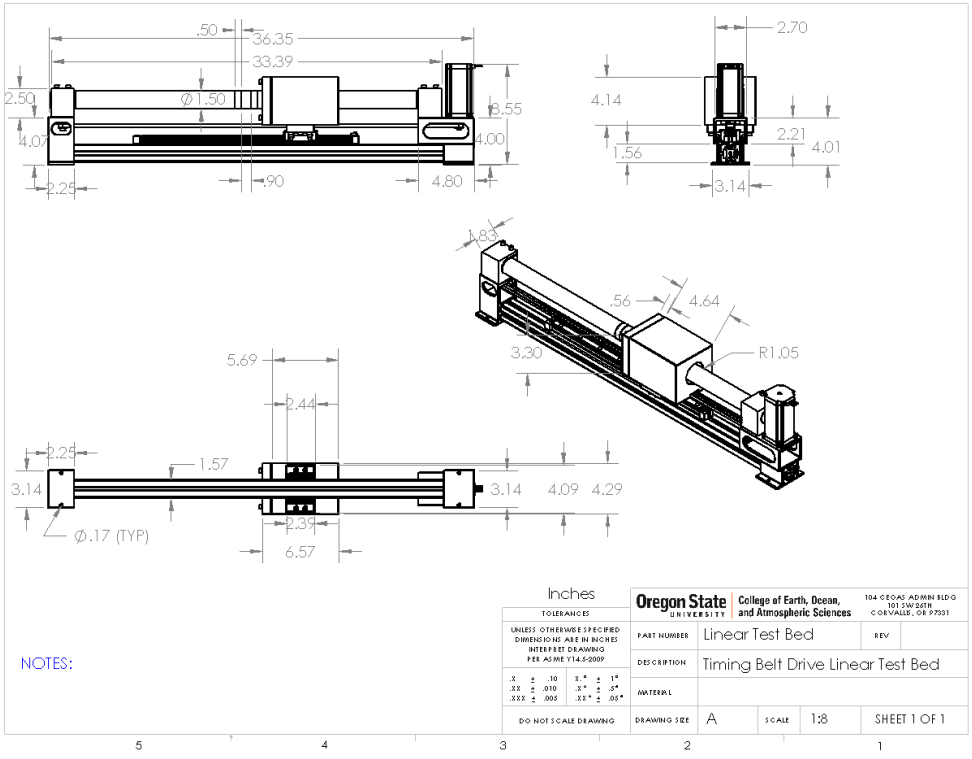

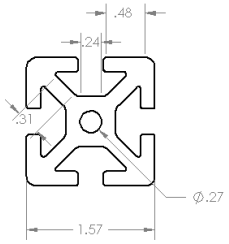

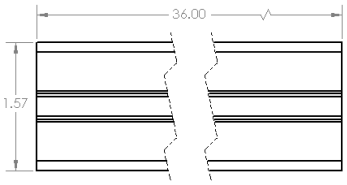

NOTES:

TOLERANCES	Oregon State University | College of Earth, Ocean, and Atmospheric Sciences		104 COAS ADMIN BLDG 101 SW 26TH CORVALLIS, OR 97331
UNLESS OTHERWISE SPECIFIED DIMENSIONS ARE IN INCHES INTERPRET DRAWING PER ASME Y14.5-2009	PART NUMBER		REV
X ± .10 X.X ± 1° XX ± .010 X.XX ± .5° XXX ± .005 XX.X ± .02 °	DESCRIPTION	Extruded Aluminum	
	MATERIAL		
DO NOT SCALE DRAWING	DRAWING SIZE	A	SCALE 1:1 SHEET 1 OF 1

5 4 3 2 1

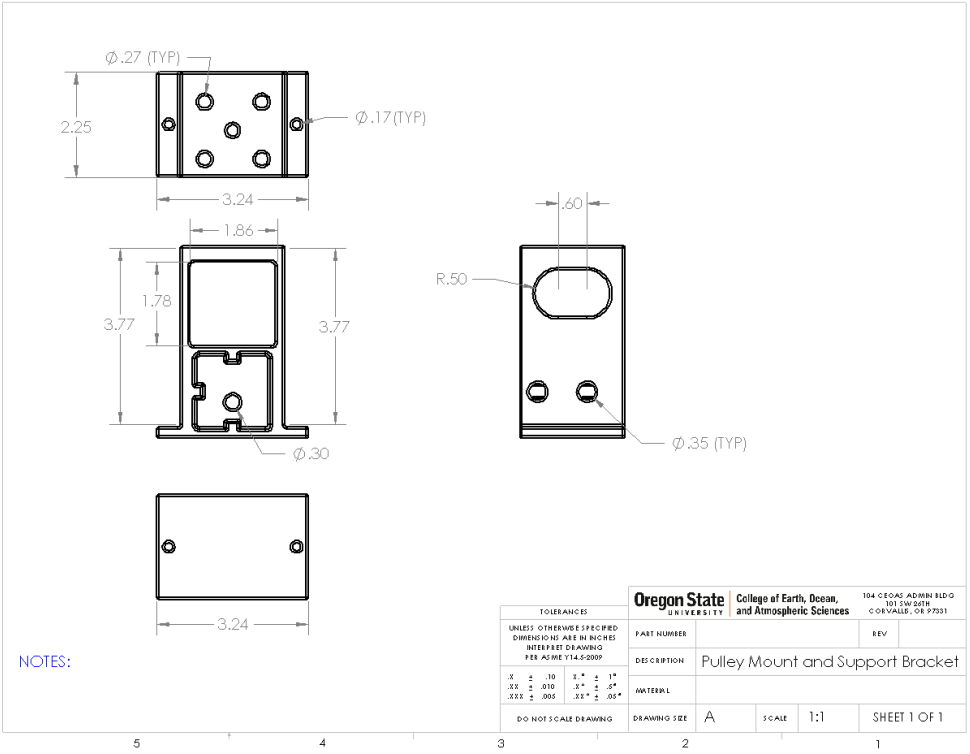
Ø.27 (TYP)
2.25
Ø.17(TYP)
3.24
1.86
1.78
3.77
3.77
Ø.30
3.24
.60
R.50
Ø.35 (TYP)
NOTES:
TOLERANCES
UNLESS OTHERWISE SPECIFIED DIMENSIONS ARE IN INCHES INTERPRET DRAWING PER ASME Y14.5-2009
DO NOT SCALE DRAWING
Oregon State UNIVERSITY
College of Earth, Ocean, and Atmospheric Sciences
104 CEOAS ADMIN BLDG
101 SW 26TH
CORVALLIS, OR 97331
PART NUMBER
REV
DESCRIPTION
Pulley Mount and Support Bracket
MATERIAL
DRAWING SIZE
A
SCALE
1:1
SHEET 1 OF 1

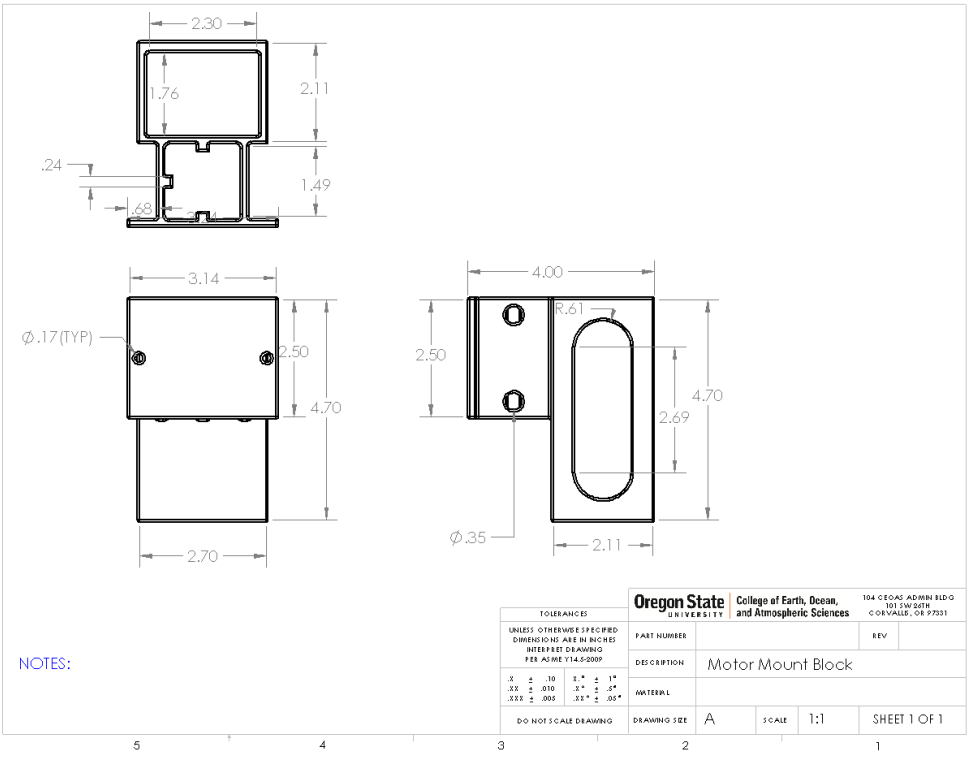

NOTES:

TOLERANCES	Oregon State UNIVERSITY College of Earth, Ocean, and Atmospheric Sciences				104 CEOAS ADMIN BLDG 101 SW 26TH CORVALLIS, OR 97331
UNLESS OTHERWISE SPECIFIED DIMENSIONS ARE IN INCHES INTERPRET DRAWING PER ASME Y14.5-2009	PART NUMBER				REV
	DESCRIPTION	Motor Mount Block			
	MATERIAL				
DO NOT SCALE DRAWING	DRAWING SIZE	A	SCALE	1:1	SHEET 1 OF 1

5 4 3 2 1

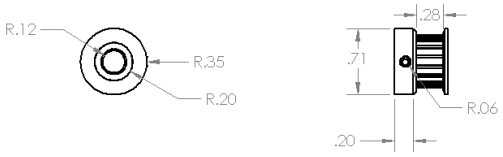

NOTES:

TOLERANCES	Oregon State UNIVERSITY College of Earth, Ocean, and Atmospheric Sciences				104 CEOAS ADMIN BLDG 101 SW 26TH CORVALLIS, OR 97331
UNLESS OTHERWISE SPECIFIED DIMENSIONS ARE IN INCHES INTERPRET DRAWING PER ASME Y14.5-2009	PART NUMBER	3 mm pulley			REV
	DESCRIPTION				
X ± .10 XX ± .010 XXX ± .005 / X° ± 1° .X° ± .5° .XX° ± .05°	MATERIAL				
DO NOT SCALE DRAWING	DRAWING SIZE	A	SCALE	1:1	SHEET 1 OF 1

5 4 3 2 1

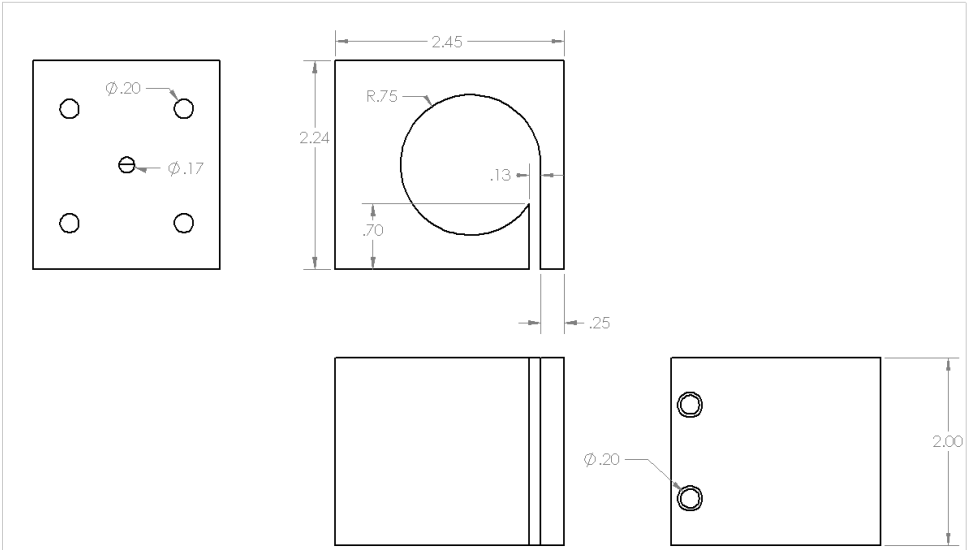

NOTES:

TOLERANCES	Oregon State UNIVERSITY College of Earth, Ocean, and Atmospheric Sciences				104 CEOAS ADMIN BLDG 101 SW 26TH CORVALLIS, OR 97331
UNLESS OTHERWISE SPECIFIED DIMENSIONS ARE IN INCHES INTERPRET DRAWING PER ASME Y14.5-2009	PART NUMBER			REV	
	DESCRIPTION	Stator Holder Clamp			
X ± .10 .XX ± .010 .XXX ± .005 / X.° ± 1° .X.° ± .5° .XX.° ± .05°	MATERIAL	Acetal			
DO NOT SCALE DRAWING	DRAWING SIZE	A	SCALE	1:1	SHEET 1 OF 1

5 4 3 2 1

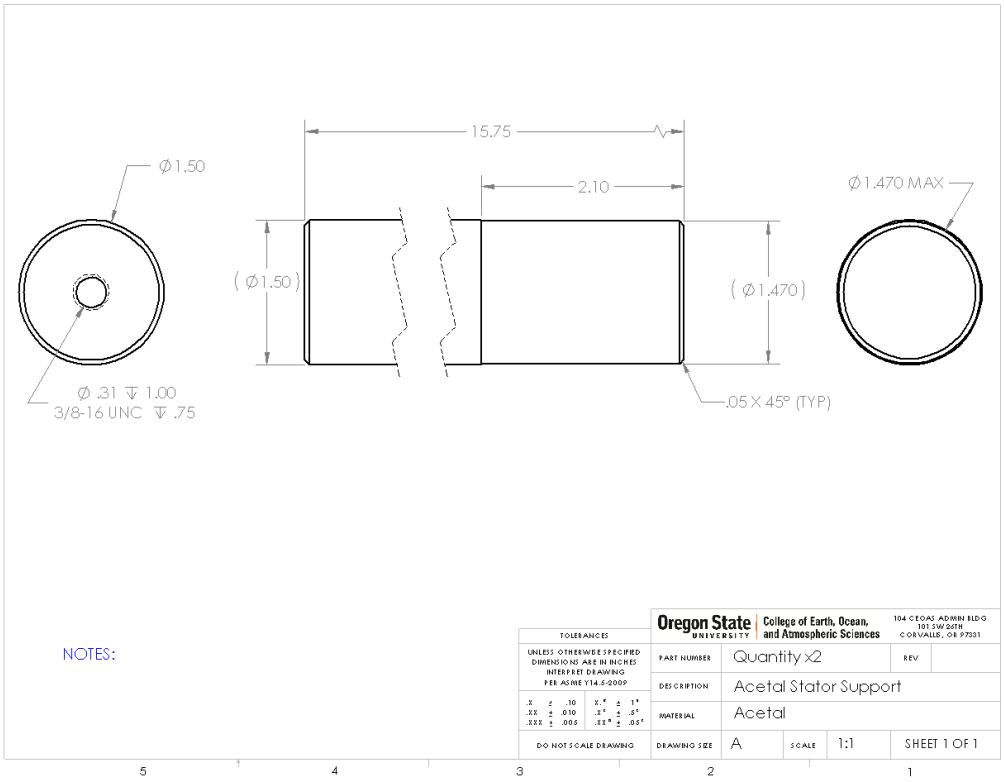

NOTES:

TOLERANCES	Oregon State University | College of Earth, Ocean, and Atmospheric Sciences			104 CEOAS ADMIN BLDG 101 SW 26TH CORVALLIS, OR 97331
UNLESS OTHERWISE SPECIFIED DIMENSIONS ARE IN INCHES INTERPRET DRAWING PER ASME Y14.5-2009	PART NUMBER	Quantity x2	REV	
.X ± .10 .X° ± 1° .XX ± .010 .X° ± .5° .XXX ± .005 .XX° ± .05°	DESCRIPTION	Acetal Stator Support		
	MATERIAL	Acetal		
DO NOT SCALE DRAWING	DRAWING SIZE	A	SCALE 1:1	SHEET 1 OF 1

5 4 3 2 1

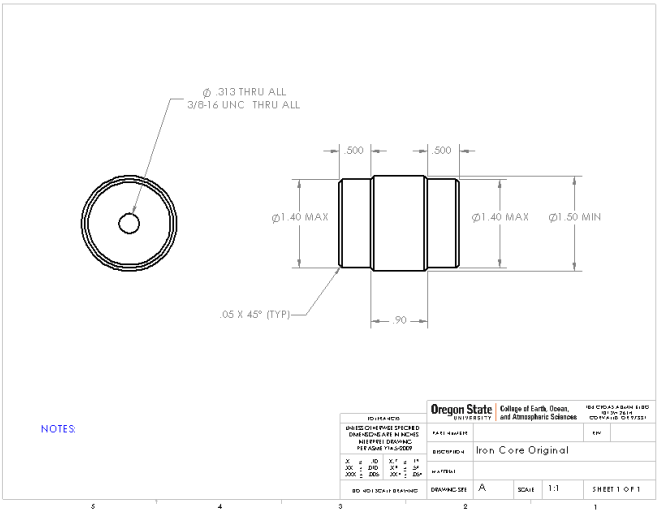
Ø .313 THRU ALL
3/8-16 UNC THRU ALL
.500
.500
Ø1.40 MAX
Ø1.40 MAX
Ø1.50 MIN
.05 X 45° (TYP)
.90
NOTES:
Oregon State University
College of Earth, Ocean, and Atmospheric Sciences
DESCRIPTION
Iron Core Original
DRAWING SIZE
A
SCALE
1:1
SHEET 1 OF 1

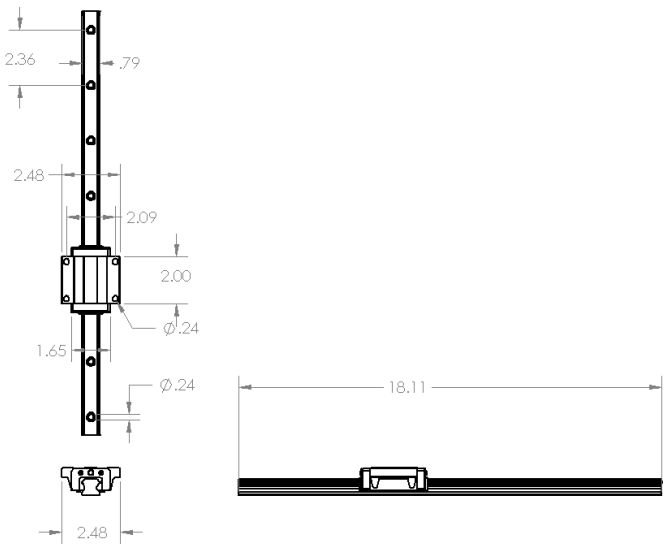

NOTES:

TOLERANCES	Oregon State UNIVERSITY College of Earth, Ocean, and Atmospheric Sciences				104 CEOAS ADMIN BLDG 101 SW 26TH CORVALLIS, OR 97331
UNLESS OTHERWISE SPECIFIED DIMENSIONS ARE IN INCHES INTERPRET DRAWING PER ASME Y14.5-2009	PART NUMBER			REV	
	DESCRIPTION	Linear Rail and Truck			
X ± .10 .XX ± .010 .XXX ± .005 X.° ± 1° .X.° ± .5° .XX.° ± .05°	MATERIAL				
DO NOT SCALE DRAWING	DRAWING SIZE	A	SCALE	1:1	SHEET 1 OF 1

5 4 3 2 1

Appendix C. Stator Redesign